UNIVERSITY OF AMSTERDAM

UvA-DARE (Digital Academic Repository)

The Polarized Image of a Synchrotron-emitting Ring of Gas Orbiting a Black Hole

Narayan, R.; Palumbo, D.C.M.; Johnson, M.D.; Gelles, Z.; Himwich, E.; Chang, D.O.; Ricarte, A.; Dexter, J.; Gammie, C.F.; Chael, A.A.; The Event Horizon Telescope Collaboration

DOI
10.3847/1538-4357/abf117

Publication date
2021

Document Version
Final published version

Published in
Astrophysical Journal

License
CC BY

Link to publication

Citation for published version (APA):
Narayan, R., Palumbo, D. C. M., Johnson, M. D., Gelles, Z., Himwich, E., Chang, D. O., Ricarte, A., Dexter, J., Gammie, C. F., Chael, A. A., & The Event Horizon Telescope Collaboration (2021). The Polarized Image of a Synchrotron-emitting Ring of Gas Orbiting a Black Hole. *Astrophysical Journal*, *912*(1), Article 35. https://doi.org/10.3847/1538-4357/abf117

General rights
It is not permitted to download or to forward/distribute the text or part of it without the consent of the author(s) and/or copyright holder(s), other than for strictly personal, individual use, unless the work is under an open content license (like Creative Commons).

Disclaimer/Complaints regulations
If you believe that digital publication of certain material infringes any of your rights or (privacy) interests, please let the Library know, stating your reasons. In case of a legitimate complaint, the Library will make the material inaccessible and/or remove it from the website. Please Ask the Library: https://uba.uva.nl/en/contact, or a letter to: Library of the University of Amsterdam, Secretariat, P.O. Box 19185, 1000 GD Amsterdam, The Netherlands. You will be contacted as soon as possible.
UvA-DARE is a service provided by the library of the University of Amsterdam (https://dare.uva.nl)

Download date:15 Oct 2026

The Astrophysical Journal, 912:35 (26pp), 2021 May 1 https://doi.org/10.3847/1538-4357/abf117
© 2021 The Author(s). Published by the American Astronomical Society.
OPEN ACCESS

The Polarized Image of a Synchrotron-emitting Ring of Gas Orbiting a Black Hole

Ramesh Narayan[1,2], Daniel C. M. Palumbo[1,2], Michael D. Johnson[1,2], Zachary Gelles[1,2], Elizabeth Himwich[2,3], Dominic O. Chang[1,2], Angelo Ricarte[1,2], Jason Dexter[4], Charles F. Gammie[5,6], Andrew A. Chael[7,123]
The Event Horizon Telescope Collaboration,
Kazunori Akiyama[2,8,9], Antxon Alberdi[10], Walter Alef[11], Juan Carlos Algaba[12], Richard Anantua[1,2], Keiichi Asada[13], Rebecca Azulay[11,14,15], Anne-Kathrin Baczko[11], David Ball[16], Mislav Baloković[1,2], John Barrett[8], Bradford A. Benson[17,18], Dan Bintley[19], Lindy Blackburn[1,2], Raymond Blundell[1], Wilfred Boland[20], Katherine L. Bouman[1,2,21], Geoffrey C. Bower[22], Hope Boyce[23,24], Michael Bremer[25], Christiaan D. Brinkerink[26], Roger Brissenden[1,2], Silke Britzen[11], Avery E. Broderick[27,28,29], Dominique Broguiere[25], Thomas Bronzwaer[26], Do-Young Byun[30,31], John E. Carlstrom[18,32,33,34], Chi-kwan Chan[16,35], Shami Chatterjee[36], Koushik Chatterjee[37], Ming-Tang Chen[22], Yongjun Chen (陈永军)[38,39], Paul M. Chesler[2], Ilje Cho[30,31], Pierre Christian[40], John E. Conway[41], James M. Cordes[36], Thomas M. Crawford[18,32], Geoffrey B. Crew[8], Alejandro Cruz-Osorio[42], Yuzhu Cui[43,44], Jordy Davelaar[26,45,46], Mariafelicia De Laurentis[42,47,48], Roger Deane[49,50,51], Jessica Dempsey[19], Gregory Desvignes[52], Sheperd S. Doeleman[1,2], Ralph P. Eatough[11,53], Heino Falcke[26], Joseph Farah[1,2,54], Vincent L. Fish[8], Ed Fomalont[55], H. Alyson Ford[56], Raquel Fraga-Encinas[26], Per Friberg[19], Christian M. Fromm[1,2,42], Antonio Fuentes[10], Peter Galison[2,57,58], Roberto García[25], Olivier Gentaz[25], Boris Georgiev[28,29], Ciriaco Goddi[26,59], Roman Gold[27,60], José L. Gómez[61], Arturo I. Gómez-Ruiz[62,63], Minfeng Gu (顾敏峰)[38,64], Mark Gurwell[1], Kazuhiro Hada[43,44], Daryl Haggard[23,24], Michael H. Hecht[8], Ronald Hesper[65], Luis C. Ho (何子山)[66,67], Paul Ho[13], Mareki Honma[43,44,68], Chih-Wei L. Huang[13], Lei Huang (黄磊)[38,64], David H. Hughes[62], Shiro Ikeda[9,69,70,71], Makoto Inoue[13], Sara Issaoun[26], David J. James[1,2], Buell T. Jannuzi[16], Michael Janssen[11], Britton Jeter[28,29], Wu Jiang (江悟)[38], Alejandra Jimenez-Rosales[26], Svetlana Jorstad[72,73], Taehyun Jung[30,31], Mansour Karami[27,28], Ramesh Karuppusamy[11], Tomohisa Kawashima[74], Garrett K. Keating[1], Mark Kettenis[75], Dong-Jin Kim[11], Jae-Young Kim[11,30], Jongsoo Kim[30], Junhan Kim[16,21], Motoki Kino[9,76], Jun Yi Koay[13], Yutaro Kofuji[43,68], Patrick M. Koch[13], Shoko Koyama[13], Michael Kramer[11], Carsten Kramer[25], Thomas P. Krichbaum[11], Cheng-Yu Kuo[77,13], Tod R. Lauer[78], Sang-Sung Lee[30], Aviad Levis[21], Yan-Rong Li (李彦荣)[79], Zhiyuan Li (李志远)[80,81], Michael Lindqvist[41], Rocco Lico[10,11], Greg Lindahl[1], Jun Liu (刘俊)[11], Kuo Liu[11], Elisabetta Liuzzo[82], Wen-Ping Lo[13,83], Andrei P. Lobanov[11], Laurent Loinard[84,85], Colin Lonsdale[8], Ru-Sen Lu (路如森)[38,39,11], Nicholas R. MacDonald[11], Jirong Mao (毛基荣)[86,87,88], Nicola Marchili[11,82], Sera Markoff[37,89], Daniel P. Marrone[16], Alan P. Marscher[72], Iván Martí-Vidal[14,15], Satoki Matsushita[13], Lynn D. Matthews[8], Lia Medeiros[16,90], Karl M. Menten[11], Izumi Mizuno[19], Yosuke Mizuno[42,91], James M. Moran[1,2], Kotaro Moriyama[8,43], Monika Moscibrodzka[26], Cornelia Müller[11,26], Gibwa Musoke[26,37], Alejandro Mus Mejías[14,15], Hiroshi Nagai[9,44], Neil M. Nagar[92], Masanori Nakamura[13,93], Gopal Narayanan[94], Iniyan Natarajan[49,51,95], Antonios Nathanail[42], Joey Neilsen[96], Roberto Neri[25], Chunchong Ni[28,29], Aristeidis Noutsos[11], Michael A. Nowak[97], Hiroki Okino[43,68], Héctor Olivares[26], Gisela N. Ortiz-León[11], Tomoaki Oyama[43], Feryal Özel[16], Jongho Park[13], Nimesh Patel[1], Ue-Li Pen[27,98,99,100], Dominic W. Pesce[1,2], Vincent Piétu[25], Richard Plambeck[101], Aleksandar PopStefanija[94], Oliver Porth[37,42], Felix M. Pötzl[11], Ben Prather[102], Jorge A. Preciado-López[27], Dimitrios Psaltis[16], Hung-Yi Pu[13,27,103], Venkatessh Ramakrishnan[92], Ramprasad Rao[22], Mark G. Rawlings[19], Alexander W. Raymond[1,2], Luciano Rezzolla[42,104,105], Bart Ripperda[45,106], Freek Roelofs[26], Alan Rogers[8], Eduardo Ros[11], Mel Rose[16], Arash Roshanineshat[16], Helge Rottmann[11], Alan L. Roy[11], Chet Ruszczyk[8], Kazi L. J. Rygl[82], Salvador Sánchez[107], David Sánchez-Arguelles[62,63], Mahito Sasada[43,108], Tuomas Savolainen[11,109,110], F. Peter Schloerb[94], Karl-Friedrich Schuster[25], Lijing Shao[11,67], Zhiqiang Shen (沈志强)[38,39], Des Small[75], Bong Won Sohn[30,31,111], Jason SooHoo[8], He Sun (孙赫)[21], Fumie Tazaki[43], Alexandra J. Tetarenko[19], Paul Tiede[28,29], Remo P. J. Tilanus[16,26,59,112], Michael Titus[8], Kenji Toma[113,114], Pablo Torne[11,107], Tyler Trent[16], Efthalia Traianou[11], Sascha Trippe[115], Ilse van Bemmel[75], Huib Jan van Langevelde[75,116], Daniel R. van Rossum[26], Jan Wagner[11], Derek Ward-Thompson[117], John Wardle[118], Jonathan Weintroub[1,2], Norbert Wex[11], Robert Wharton[11], Maciek Wielgus[1,2], George N. Wong[102], Qingwen Wu (吴庆文)[119], Doosoo Yoon[37], André Young[26], Ken Young[1], Ziri Younsi[42,120,124], Feng Yuan (袁峰)[38,64,121], Ye-Fei Yuan (袁业飞)[122], J. Anton Zensus[11], Guang-Yao Zhao[10], and Shan-Shan Zhao[38]

[1] Center for Astrophysics, Harvard & Smithsonian, 60 Garden Street, Cambridge, MA 02138, USA
[2] Black Hole Initiative at Harvard University, 20 Garden Street, Cambridge, MA 02138, USA
[3] Center for the Fundamental Laws of Nature, Harvard University, Cambridge, MA 02138, USA
[4] JILA and Department of Astrophysical and Planetary Sciences, University of Colorado, Boulder, CO 80309, USA
[5] Department of Physics, University of Illinois at Urbana-Champaign, 1110 West Green Street, Urbana, IL 61801, USA
[6] Department of Astronomy, University of Illinois at Urbana-Champaign, 1002 West Green Street, Urbana, IL 61801, USA
[7] Princeton Center for Theoretical Science, Jadwin Hall, Princeton University, Princeton, NJ 08544, USA
[8] Massachusetts Institute of Technology Haystack Observatory, 99 Millstone Road, Westford, MA 01886, USA
[9] National Astronomical Observatory of Japan, 2-21-1 Osawa, Mitaka, Tokyo 181-8588, Japan
[10] Instituto de Astrofísica de Andalucía-CSIC, Glorieta de la Astronomía s/n, E-18008 Granada, Spain
[11] Max-Planck-Institut für Radioastronomie, Auf dem Hügel 69, D-53121 Bonn, Germany
[12] Department of Physics, Faculty of Science, University of Malaya, 50603 Kuala Lumpur, Malaysia
[13] Institute of Astronomy and Astrophysics, Academia Sinica, 11F of Astronomy-Mathematics Building, AS/NTU No. 1, Sec. 4, Roosevelt Rd., Taipei 10617, Taiwan, R.O.C.

This is an open access article distributed under the terms of the Creative Commons Attribution 4.0 License.
Any further distribution of this work must maintain attribution to the author(s) and the title of the work, journal citation and DOI.

[14] Departament d'Astronomia i Astrofísica, Universitat de València, C. Dr. Moliner 50, E-46100 Burjassot, València, Spain
[15] Observatori Astronòmic, Universitat de València, C. Catedrático José Beltrán 2, E-46980 Paterna, València, Spain
[16] Steward Observatory and Department of Astronomy, University of Arizona, 933 N. Cherry Avenue, Tucson, AZ 85721, USA
[17] Fermi National Accelerator Laboratory, MS209, P.O. Box 500, Batavia, IL 60510, USA
[18] Department of Astronomy and Astrophysics, University of Chicago, 5640 South Ellis Avenue, Chicago, IL 60637, USA
[19] East Asian Observatory, 660 N. A'ohoku Place, Hilo, HI 96720, USA
[20] Nederlandse Onderzoekschool voor Astronomie (NOVA), PO Box 9513, 2300 RA Leiden, The Netherlands
[21] California Institute of Technology, 1200 East California Boulevard, Pasadena, CA 91125, USA
[22] Institute of Astronomy and Astrophysics, Academia Sinica, 645 N. A'ohoku Place, Hilo, HI 96720, USA
[23] Department of Physics, McGill University, 3600 rue University, Montréal, QC H3A 2T8, Canada
[24] McGill Space Institute, McGill University, 3550 rue University, Montréal, QC H3A 2A7, Canada
[25] Institut de Radioastronomie Millimétrique, 300 rue de la Piscine, F-38406 Saint Martin d'Hères, France
[26] Department of Astrophysics, Institute for Mathematics, Astrophysics and Particle Physics (IMAPP), Radboud University, P.O. Box 9010, 6500 GL Nijmegen, The Netherlands
[27] Perimeter Institute for Theoretical Physics, 31 Caroline Street North, Waterloo, ON N2L 2Y5, Canada
[28] Department of Physics and Astronomy, University of Waterloo, 200 University Avenue West, Waterloo, ON N2L 3G1, Canada
[29] Waterloo Centre for Astrophysics, University of Waterloo, Waterloo, ON N2L 3G1, Canada
[30] Korea Astronomy and Space Science Institute, Daedeok-daero 776, Yuseong-gu, Daejeon 34055, Republic of Korea
[31] University of Science and Technology, Gajeong-ro 217, Yuseong-gu, Daejeon 34113, Republic of Korea
[32] Kavli Institute for Cosmological Physics, University of Chicago, 5640 South Ellis Avenue, Chicago, IL 60637, USA
[33] Department of Physics, University of Chicago, 5720 South Ellis Avenue, Chicago, IL 60637, USA
[34] Enrico Fermi Institute, University of Chicago, 5640 South Ellis Avenue, Chicago, IL 60637, USA
[35] Data Science Institute, University of Arizona, 1230 N. Cherry Avenue, Tucson, AZ 85721, USA
[36] Cornell Center for Astrophysics and Planetary Science, Cornell University, Ithaca, NY 14853, USA
[37] Anton Pannekoek Institute for Astronomy, University of Amsterdam, Science Park 904, 1098 XH, Amsterdam, The Netherlands
[38] Shanghai Astronomical Observatory, Chinese Academy of Sciences, 80 Nandan Road, Shanghai 200030, People's Republic of China
[39] Key Laboratory of Radio Astronomy, Chinese Academy of Sciences, Nanjing 210008, People's Republic of China
[40] Physics Department, Fairfield University, 1073 North Benson Road, Fairfield, CT 06824, USA
[41] Department of Space, Earth and Environment, Chalmers University of Technology, Onsala Space Observatory, SE-43992 Onsala, Sweden
[42] Institut für Theoretische Physik, Goethe-Universität Frankfurt, Max-von-Laue-Straße 1, D-60438 Frankfurt am Main, Germany
[43] Mizusawa VLBI Observatory, National Astronomical Observatory of Japan, 2-12 Hoshigaoka, Mizusawa, Oshu, Iwate 023-0861, Japan
[44] Department of Astronomical Science, The Graduate University for Advanced Studies (SOKENDAI), 2-21-1 Osawa, Mitaka, Tokyo 181-8588, Japan
[45] Center for Computational Astrophysics, Flatiron Institute, 162 Fifth Avenue, New York, NY 10010, USA
[46] Department of Astronomy and Columbia Astrophysics Laboratory, Columbia University, 550 W. 120th Street, New York, NY 10027, USA
[47] Dipartimento di Fisica "E. Pancini," Universitá di Napoli "Federico II," Compl. Univ. di Monte S. Angelo, Edificio G, Via Cinthia, I-80126, Napoli, Italy
[48] INFN Sez. di Napoli, Compl. Univ. di Monte S. Angelo, Edificio G, Via Cinthia, I-80126, Napoli, Italy
[49] Wits Centre for Astrophysics, University of the Witwatersrand, 1 Jan Smuts Avenue, Braamfontein, Johannesburg 2050, South Africa
[50] Department of Physics, University of Pretoria, Hatfield, Pretoria 0028, South Africa
[51] Centre for Radio Astronomy Techniques and Technologies, Department of Physics and Electronics, Rhodes University, Makhanda 6140, South Africa
[52] LESIA, Observatoire de Paris, Université PSL, CNRS, Sorbonne Université, Université de Paris, 5 place Jules Janssen, F-92195 Meudon, France
[53] National Astronomical Observatories, Chinese Academy of Sciences, 20A Datun Road, Chaoyang District, Beijing 100101, People's Republic of China
[54] University of Massachusetts Boston, 100 William T. Morrissey Boulevard, Boston, MA 02125, USA
[55] National Radio Astronomy Observatory, 520 Edgemont Rd., Charlottesville, VA 22903, USA
[56] Steward Observatory and Department of Astronomy, University of Arizona, 933 N. Cherry Avenue, Tucson, AZ 85721, USA
[57] Department of History of Science, Harvard University, Cambridge, MA 02138, USA
[58] Department of Physics, Harvard University, Cambridge, MA 02138, USA
[59] Leiden Observatory—Allegro, Leiden University, P.O. Box 9513, 2300 RA Leiden, The Netherlands
[60] CP3-Origins, University of Southern Denmark, Campusvej 55, DK-5230 Odense M, Denmark
[61] Instituto de Astrofísica de Andalucía-CíSIC, Glorieta de la Astronomía s/n, E-18008 Granada, Spain
[62] Instituto Nacional de Astrofísica, Óptica y Electrónica. Apartado Postal 51 y 216, 72000. Puebla Pue., Mexico
[63] Consejo Nacional de Ciencia y Tecnología, Av. Insurgentes Sur 1582, 03940, Ciudad de México, Mexico
[64] Key Laboratory for Research in Galaxies and Cosmology, Chinese Academy of Sciences, Shanghai 200030, People's Republic of China
[65] NOVA Sub-mm Instrumentation Group, Kapteyn Astronomical Institute, University of Groningen, Landleven 12, 9747 AD Groningen, The Netherlands
[66] Department of Astronomy, School of Physics, Peking University, Beijing 100871, People's Republic of China
[67] Kavli Institute for Astronomy and Astrophysics, Peking University, Beijing 100871, People's Republic of China
[68] Department of Astronomy, Graduate School of Science, The University of Tokyo, 7-3-1 Hongo, Bunkyo-ku, Tokyo 113-0033, Japan
[69] The Institute of Statistical Mathematics, 10-3 Midori-cho, Tachikawa, Tokyo, 190-8562, Japan
[70] Department of Statistical Science, The Graduate University for Advanced Studies (SOKENDAI), 10-3 Midori-cho, Tachikawa, Tokyo 190-8562, Japan
[71] Kavli Institute for the Physics and Mathematics of the Universe, The University of Tokyo, 5-1-5 Kashiwanoha, Kashiwa, 277-8583, Japan
[72] Institute for Astrophysical Research, Boston University, 725 Commonwealth Avenue, Boston, MA 02215, USA
[73] Astronomical Institute, St. Petersburg University, Universitetskij pr., 28, Petrodvorets,198504 St. Petersburg, Russia
[74] Institute for Cosmic Ray Research, The University of Tokyo, 5-1-5 Kashiwanoha, Kashiwa, Chiba 277-8582, Japan
[75] Joint Institute for VLBI ERIC (JIVE), Oude Hoogeveensedijk 4, 7991 PD Dwingeloo, The Netherlands
[76] Kogakuin University of Technology & Engineering, Academic Support Center, 2665-1 Nakano, Hachioji, Tokyo 192-0015, Japan
[77] Physics Department, National Sun Yat-Sen University, No. 70, Lien-Hai Rd., Kaosiung City 80424, Taiwan, R.O.C
[78] National Optical Astronomy Observatory, 950 N. Cherry Avenue, Tucson, AZ 85719, USA
[79] Key Laboratory for Particle Astrophysics, Institute of High Energy Physics, Chinese Academy of Sciences, 19B Yuquan Road, Shijingshan District, Beijing, People's Republic of China
[80] School of Astronomy and Space Science, Nanjing University, Nanjing 210023, People's Republic of China
[81] Key Laboratory of Modern Astronomy and Astrophysics, Nanjing University, Nanjing 210023, People's Republic of China
[82] Italian ALMA Regional Centre, INAF-Istituto di Radioastronomia, Via P. Gobetti 101, I-40129 Bologna, Italy
[83] Department of Physics, National Taiwan University, No. 1, Sect. 4, Roosevelt Road, Taipei 10617, Taiwan, R.O.C
[84] Instituto de Radioastronomía y Astrofísica, Universidad Nacional Autónoma de México, Morelia 58089, Mexico
[85] Instituto de Astronomía, Universidad Nacional Autónoma de México, CdMx 04510, Mexico
[86] Yunnan Observatories, Chinese Academy of Sciences, 650011 Kunming, Yunnan Province, People's Republic of China
[87] Center for Astronomical Mega-Science, Chinese Academy of Sciences, 20A Datun Road, Chaoyang District, Beijing, 100012, People's Republic of China

[88] Key Laboratory for the Structure and Evolution of Celestial Objects, Chinese Academy of Sciences, 650011 Kunming, People's Republic of China
[89] Gravitation Astroparticle Physics Amsterdam (GRAPPA) Institute, University of Amsterdam, Science Park 904, 1098 XH Amsterdam, The Netherlands
[90] School of Natural Sciences, Institute for Advanced Study, 1 Einstein Drive, Princeton, NJ 08540, USA
[91] Tsung-Dao Lee Institute and School of Physics and Astronomy, Shanghai Jiao Tong University, Shanghai, 200240, People's Republic of China
[92] Astronomy Department, Universidad de Concepción, Casilla 160-C, Concepción, Chile
[93] National Institute of Technology, Hachinohe College, 16-1 Uwanotai, Tamonoki, Hachinohe City, Aomori 039-1192, Japan
[94] Department of Astronomy, University of Massachusetts, Amherst, MA 01003, USA
[95] South African Radio Astronomy Observatory, Observatory 7925, Cape Town, South Africa
[96] Villanova University, Mendel Science Center Rm. 263B, 800 E. Lancaster Avenue, Villanova PA 19085, USA
[97] Physics Department, Washington University CB 1105, St Louis, MO 63130, USA
[98] Canadian Institute for Theoretical Astrophysics, University of Toronto, 60 St. George Street, Toronto, ON M5S 3H8, Canada
[99] Dunlap Institute for Astronomy and Astrophysics, University of Toronto, 50 St. George Street, Toronto, ON M5S 3H4, Canada
[100] Canadian Institute for Advanced Research, 180 Dundas St. West, Toronto, ON M5G 1Z8, Canada
[101] Radio Astronomy Laboratory, University of California, Berkeley, CA 94720, USA
[102] Department of Physics, University of Illinois, 1110 West Green Street, Urbana, IL 61801, USA
[103] Department of Physics, National Taiwan Normal University, No. 88, Sec. 4, Tingzhou Road, Taipei 116, Taiwan, R.O.C.
[104] Frankfurt Institute for Advanced Studies, Ruth-Moufang-Strasse 1, D-60438 Frankfurt, Germany
[105] School of Mathematics, Trinity College, Dublin 2, Ireland
[106] Department of Astrophysical Sciences, Peyton Hall, Princeton University, Princeton, NJ 08544, USA
[107] Instituto de Radioastronomía Milimétrica, IRAM, Avenida Divina Pastora 7, Local 20, E-18012, Granada, Spain
[108] Hiroshima Astrophysical Science Center, Hiroshima University, 1-3-1 Kagamiyama, Higashi-Hiroshima, Hiroshima 739-8526, Japan
[109] Aalto University Department of Electronics and Nanoengineering, PL 15500, FI-00076 Aalto, Finland
[110] Aalto University Metsähovi Radio Observatory, Metsähovintie 114, FI-02540 Kylmälä, Finland
[111] Department of Astronomy, Yonsei University, Yonsei-ro 50, Seodaemun-gu, 03722 Seoul, Republic of Korea
[112] Netherlands Organisation for Scientific Research (NWO), Postbus 93138, 2509 AC Den Haag, The Netherlands
[113] Frontier Research Institute for Interdisciplinary Sciences, Tohoku University, Sendai 980-8578, Japan
[114] Astronomical Institute, Tohoku University, Sendai 980-8578, Japan
[115] Department of Physics and Astronomy, Seoul National University, Gwanak-gu, Seoul 08826, Republic of Korea
[116] Leiden Observatory, Leiden University, Postbus 2300, 9513 RA Leiden, The Netherlands
[117] Jeremiah Horrocks Institute, University of Central Lancashire, Preston PR1 2HE, UK
[118] Physics Department, Brandeis University, 415 South Street, Waltham, MA 02453, USA
[119] School of Physics, Huazhong University of Science and Technology, Wuhan, Hubei, 430074, People's Republic of China
[120] Mullard Space Science Laboratory, University College London, Holmbury St. Mary, Dorking, Surrey, RH5 6NT, UK
[121] School of Astronomy and Space Sciences, University of Chinese Academy of Sciences, No. 19A Yuquan Road, Beijing 100049, People's Republic of China
[122] Astronomy Department, University of Science and Technology of China, Hefei 230026, People's Republic of China
Received 2021 January 31; revised 2021 March 18; accepted 2021 March 21; published 2021 May 3

Abstract

Synchrotron radiation from hot gas near a black hole results in a polarized image. The image polarization is determined by effects including the orientation of the magnetic field in the emitting region, relativistic motion of the gas, strong gravitational lensing by the black hole, and parallel transport in the curved spacetime. We explore these effects using a simple model of an axisymmetric, equatorial accretion disk around a Schwarzschild black hole. By using an approximate expression for the null geodesics derived by Beloborodov and conservation of the Walker–Penrose constant, we provide analytic estimates for the image polarization. We test this model using currently favored general relativistic magnetohydrodynamic simulations of M87*, using ring parameters given by the simulations. For a subset of these with modest Faraday effects, we show that the ring model broadly reproduces the polarimetric image morphology. Our model also predicts the polarization evolution for compact flaring regions, such as those observed from Sgr A* with GRAVITY. With suitably chosen parameters, our simple model can reproduce the EVPA pattern and relative polarized intensity in Event Horizon Telescope images of M87*. Under the physically motivated assumption that the magnetic field trails the fluid velocity, this comparison is consistent with the clockwise rotation inferred from total intensity images.

Unified Astronomy Thesaurus concepts: Accretion (14); Black holes (162); Polarimetry (1278); Magnetic fields (994)

1. Introduction

The Event Horizon Telescope (EHT) Collaboration has recently published the first images of a black hole (Event Horizon Telescope Collaboration et al. 2019a, 2019b, 2019c, 2019d, 2019e, 2019f, 2021a, 2021b, hereafter EHTC I–VIII, respectively). These images achieve a diffraction-limited angular resolution that corresponds to approximately $5GM/c^2$, where M is the mass of the black hole. They reveal a bright ring of emission with a twisting polarization pattern and a prominent rotationally symmetric mode.

The polarization structure in the EHT images depends on details of the emitting plasma, principally the magnetic field geometry. However, it is also affected by the strongly curved spacetime near the black hole. Over the past few decades, simulated polarimetric images of black holes have been studied as a means to understand astrophysical properties of their surrounding accretion flows (e.g., Bromley et al. 2001; Shcherbakov et al. 2012; Mościbrodzka et al. 2017; Jiménez-Rosales & Dexter 2018; Palumbo et al. 2020) and to infer the disk inclination and black hole spin through the effects of parallel transport (e.g., Connors et al. 1980; Broderick &

[123] NASA Hubble Fellowship Program, Einstein Fellow.
[124] UKRI Stephen Hawking Fellow.

Loeb 2006; Li et al. 2009; Schnittman & Krolik 2009; Gold et al. 2017; Marin et al. 2018).

While they are becoming increasingly realistic, these simulations are generally difficult to use for broad parameter surveys because of their computational cost, and they often provide little insight into how to decouple astrophysical and relativistic effects.

In this article, we develop a simple toy model to understand polarimetric images of black holes. This model consists of a ring of magnetized fluid orbiting a Schwarzschild black hole. Our model allows arbitrary emission radius, magnetic field geometry, equatorial fluid velocity, and observer inclination. With a single approximation, described in Section 2, we can analytically compute the resulting polarimetric image and can assess its dependence on the input parameters.

In Section 2, we describe the toy ring model and work out the relevant relativistic transformations from the frame of a radiating fluid element in the ring to the image as seen on the sky by an observer. In Section 3, we present a series of examples to illustrate the primary model features. In Section 4, we provide analytic estimates of image diagnostics—the apparent shape of the ring, the vector polarization, and the coefficient of rotational symmetry (β_2; Palumbo et al. 2020). In Section 5, we discuss the suitability of our model for comparisons with observations, focusing on the EHT images of M87* and polarization "loops" seen during flares of Sagittarius A* (Sgr A*). In Section 6, we summarize our results.

2. The Model

We consider an accretion disk around a Schwarzschild black hole of mass M. We use standard geometrized units: $G = c = 1$. The fluid radiates from the equatorial plane within a narrow range of radii centered on a dimensionless radius R, measured in units of M (or GM/c^2, including the physical constants). With respect to a distant observer, the ring is tilted from a face-on orientation by an angle θ_o. We assume that the tilt is toward the North, so that the line-of-nodes between the ring orbital plane and the observer's sky plane is in the east–west direction. We take the sky angular coordinate x to be oriented toward the West (i.e., to the right), and the coordinate y toward the North (i.e., toward the top). The fluid has radial and tangential components of velocity in the plane of the ring, but no vertical velocity. In the comoving frame of the fluid, the magnetic field has radial, azimuthal and vertical components. For simplicity, we assume that both the velocity field and the magnetic field are axisymmetric, though the equations developed in this section are valid even without this assumption.

We wish to compute the following primary observables: (1) the shape of the ring as viewed by the distant observer, (2) the variation of the polarized intensity around the observed ring, and (3) the orientation and pattern of the polarization vectors around the ring. An exact calculation requires integrating the geodesic equation, which has to be done numerically. However, with one simplification, described below, it is possible to do all the calculations analytically. This simplified model provides a convenient method for investigating polarization properties of idealized models.

2.1. Geometry, Lensing and Special Relativity

In the ring plane, we consider a fluid element P located at azimuthal angle ϕ measured from the line-of-nodes. We are interested in a null geodesic, a light ray, that travels from P to the observer. This geodesic lies in a plane that includes the line from the black hole O to the point P, as well as the line from O to the observer (see Figure 1). We set up Cartesian coordinates in the geodesic plane so that the unit vector along the x-axis $\hat{x}$ is oriented along OP and the observer lies on the $\hat{x}$–$\hat{z}$ plane. We call this the geodesic frame, or G-frame. The angle ψ between $\hat{x}$ and the unit vector $\hat{n}$ toward the observer satisfies

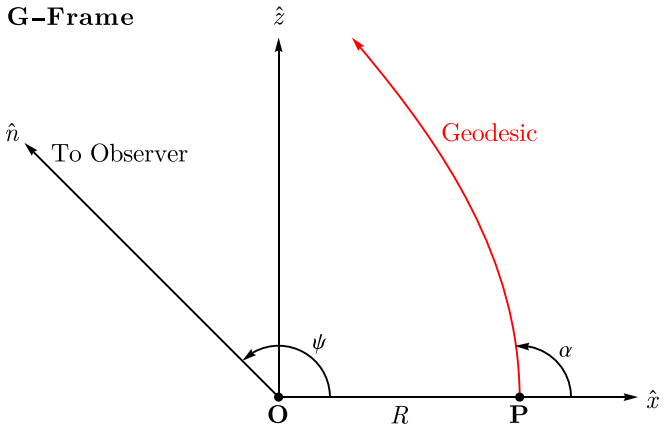

Figure 1. Geometry in the geodesic frame, or G-frame. In the Schwarzschild metric, each null geodesic is confined to a plane that intersects the black hole. The G-frame, defined for photons emitted at point P and reaching a distant observer at relative angle ψ, corresponds to Cartesian axes centered on the black hole, with $\hat{x}$ in the direction of P and the $\hat{x}$–$\hat{z}$ plane given by the geodesic plane. We approximate the emission angle α in this frame using Equation (4).

$$\cos\psi = -\sin\theta_o \sin\phi,$$
$$\sin\psi = (1 - \cos^2\psi)^{1/2}. \quad (1)$$

We consider a null geodesic with conserved energy[125] $k_t = -1$ traveling from P to the observer. At the location P, the orthonormal time component $k^{\hat{t}}_{(G)}$ of its 4-wavevector is given by (the redshift factor here is calculated using the Schwarzschild metric, as appropriate for the assumed non-spinning black hole)

$$k^{\hat{t}}_{(G)} = -\frac{k_t}{\sqrt{-g_{tt}}} = \frac{1}{\left(1 - \frac{2}{R}\right)^{1/2}}, \quad (2)$$

where the subscript "(G)" indicates that this quantity is measured in the G-frame. Also, since the geodesic lies in the xz-plane, we have $k^{\hat{y}}_{(G)} = 0$. To determine the other two components of k, we need the angle α in Figure 1, in terms of which we can write

$$k^{\hat{x}}_{(G)} = k^{\hat{t}}_{(G)} \cos\alpha, \qquad k^{\hat{z}}_{(G)} = k^{\hat{t}}_{(G)} \sin\alpha. \quad (3)$$

Instead of attempting to calculate α precisely, which would require a numerical integration of the geodesic equation, we use the following approximate formula obtained by Beloborodov (2002),

$$\cos\alpha = \cos\psi + \frac{2}{R}(1 - \cos\psi),$$
$$\sin\alpha = (1 - \cos^2\alpha)^{1/2}. \quad (4)$$

This approximation is surprisingly accurate even for values of R of order a few (see Section 3.6 and Appendix A).

[125] This is the photon energy measured by an observer at infinity, and we normalize it to unity.

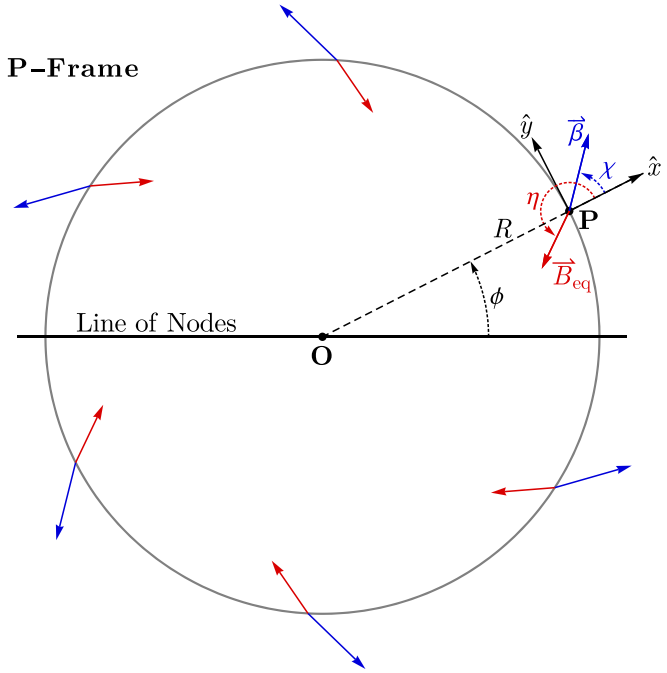

Figure 2. Geometry in the P-frame. This frame is aligned with the rotating gas at emission radius R and emission azimuth ϕ. The $\hat{x}$ direction lies along the radial line from the black hole at O to the emission point P, and $\hat{y}$ is the azimuthal direction. The equatorial magnetic field $\boldsymbol{B}_{\rm eq}$ and fluid velocity $\boldsymbol{\beta}$ lie at angles η and χ to $\hat{x}$ in the x-y plane, respectively. Our model allows these angles to be specified independently, but we will later focus on the physically motivated choices of $\eta = \chi$ and $\eta = \chi + \pi$ (see Section 3).

We now switch to a Cartesian frame that is aligned with the orbiting fluid ring. We take $\hat{x}$ along OP, $\hat{y}$ in the azimuthal direction at P parallel to $\hat{\phi}$, and $\hat{z}$ perpendicular to the orbital plane. We call this the P-frame (see Figure 2). The G-frame and P-frame have a common $\hat{x}$-axis. Therefore, transforming from one to the other involves rotation by some angle ξ around the x-axis. To determine ξ, we note that the unit vector $\hat{n}$ from the black hole O toward the observer has Cartesian components $(\cos\psi,\ 0,\ \sin\psi)$ in the G-frame, and Cartesian components $(-\sin\theta_{\rm o}\sin\phi,\ -\sin\theta_{\rm o}\cos\phi,\ \cos\theta_{\rm o})$ in the P-frame. Since a rotation by angle ξ transforms one set of components to the other, we obtain

$$\cos\xi = \frac{\cos\theta_{\rm o}}{\sin\psi}, \qquad \sin\xi = \frac{\sin\theta_{\rm o}\cos\phi}{\sin\psi}. \tag{5}$$

Applying this rotation to the orthonormal components of $k_{\rm (G)}$, we obtain the corresponding orthonormal components in the P-frame,

$$k^{\hat{t}}_{\rm (P)} = \frac{1}{\left(1-\frac{2}{R}\right)^{1/2}}, \qquad k^{\hat{x}}_{\rm (P)} = \frac{\cos\alpha}{\left(1-\frac{2}{R}\right)^{1/2}}, \tag{6}$$

$$k^{\hat{y}}_{\rm (P)} = -\frac{\sin\xi\sin\alpha}{\left(1-\frac{2}{R}\right)^{1/2}}, \qquad k^{\hat{z}}_{\rm (P)} = \frac{\cos\xi\sin\alpha}{\left(1-\frac{2}{R}\right)^{1/2}}. \tag{7}$$

The fluid at the point P moves in the xy-plane of the local P-frame with a velocity $\boldsymbol{\beta}$, which we write in the local Cartesian coordinate frame as (see Figure 2)

$$\boldsymbol{\beta} = \beta(\cos\chi\,\hat{x} + \sin\chi\,\hat{y}). \tag{8}$$

Our sign convention is that radial motion toward the black hole corresponds to $\cos\chi < 0$, and clockwise rotation on the sky corresponds to $\sin\chi < 0$. In the case of M87*, the rotation is clockwise. The velocity $\boldsymbol{\beta}$ describes motion of the fluid through the ring; the ring model itself is not expanding or contracting.

We now transform to the fluid frame—the F-frame—by applying a Lorentz boost with velocity $\boldsymbol{\beta}$. This gives the following orthonormal components of k,

$$\begin{aligned}
k^{\hat{t}}_{\rm (F)} &= \gamma\, k^{\hat{t}}_{\rm (P)} - \gamma\beta\cos\chi\, k^{\hat{x}}_{\rm (P)} - \gamma\beta\sin\chi\, k^{\hat{y}}_{\rm (P)},\\
k^{\hat{x}}_{\rm (F)} &= -\gamma\beta\cos\chi\, k^{\hat{t}}_{\rm (P)} + (1+(\gamma-1)\cos^2\chi)k^{\hat{x}}_{\rm (P)}\\
&\quad + (\gamma-1)\cos\chi\sin\chi\, k^{\hat{y}}_{\rm (P)},\\
k^{\hat{y}}_{\rm (F)} &= -\gamma\beta\sin\chi\, k^{\hat{t}}_{\rm (P)} + (\gamma-1)\cos\chi\sin\chi\, k^{\hat{x}}_{\rm (P)}\\
&\quad + (1+(\gamma-1)\sin^2\chi)k^{\hat{y}}_{\rm (P)},\\
k^{\hat{z}}_{\rm (F)} &= k^{\hat{z}}_{\rm (P)}.
\end{aligned} \tag{9}$$

2.2. Transformation of Polarized Intensity

Any radiation emitted along $k^{\hat{\mu}}_{\rm (F)}$ in the F-frame is Doppler-shifted by the time it reaches the observer. Since $k^{\hat{t}}_{\rm (O)}$ in the observer frame is equal to unity, the Doppler factor δ is

$$\delta = \frac{k^{\hat{t}}_{\rm (O)}}{k^{\hat{t}}_{\rm (F)}} = \frac{1}{k^{\hat{t}}_{\rm (F)}}. \tag{10}$$

This includes both gravitational redshift and Doppler shift from velocity.

In the fluid frame, there is a magnetic field which we write as[126]

$$\begin{aligned}
\boldsymbol{B} &= B_r\hat{x} + B_\phi\hat{y} + B_z\hat{z}\\
&= B_{\rm eq}(\cos\eta\,\hat{x} + \sin\eta\,\hat{y}) + B_z\,\hat{z}\\
&\equiv \boldsymbol{B}_{\rm eq} + B_z\hat{z},
\end{aligned} \tag{11}$$

where the second line describes the field components in the equatorial plane in terms of a magnitude $B_{\rm eq}$ and an orientation η (see Figure 2). The intensity of synchrotron radiation emitted along the 3-vector $\boldsymbol{k}_{\rm (F)}$ depends on $\sin\zeta$, where ζ is the angle between $\boldsymbol{k}_{\rm (F)}$ and the magnetic field $\boldsymbol{B}$:

$$\sin\zeta = \frac{|\boldsymbol{k}_{\rm (F)}\times\boldsymbol{B}|}{|\boldsymbol{k}_{\rm (F)}|\,|\boldsymbol{B}|}. \tag{12}$$

In the case of thermal synchrotron emission, the intensity also depends on the ratio of the emitted photon energy $h\nu$ to the electron temperature kT_e. At low frequencies $h\nu \ll kT_e$, the intensity is proportional to $\sin^{2/3}\zeta$ (e.g., Mahadevan et al. 1996), whereas in the opposite limit $h\nu \gg kT_e$, the intensity varies as a very large positive power of $\sin\zeta$, because of the exponential cutoff of the particle energy distribution and the corresponding rapid decline of emissivity with increasing frequency. In general, if the emitted intensity varies as $I_\nu \sim \nu^{-\alpha_\nu}$, then the angle dependence goes as $(\sin\zeta)^{1+\alpha_\nu}$. In models of M87*, a dependence $\sim\sin^2\zeta$ is often obtained at 230 GHz. This corresponds to $\alpha_\nu \sim 1$, which is consistent with the synchrotron emission being close to its peak at this frequency (νF_ν roughly constant). In the analysis below, we

[126] Because the emission of synchrotron radiation is best described in the fluid frame, we find it convenient to specify the magnetic field components in this frame. The $\hat{x}$, $\hat{y}$, $\hat{z}$ axes in the fluid frame are related to the corresponding axes in the P-frame (equivalently, the Schwarzschild frame, e.g., Equation (19)), via a Lorentz transformation with velocity $\boldsymbol{\beta}$. The transformation of field components between the two frames is worked out in Appendix B.

explicitly retain the α_ν dependence. However, we set $\alpha_\nu = 1$ for the numerical calculations described in Section 3, and also when we series-expand the equations in Appendix D.

The factor $(\sin\zeta)^{1+\alpha_\nu}$ discussed in the previous paragraph is the emission per unit volume. To convert this to the emerging intensity in the fluid frame we need to multiply by the geodesic path length $l_{\rm p}$ through the emitting region. We assume that the medium is optically thin to its own emission. If we model the emitting fluid as a thin disk of vertical thickness H, then the path length is

$$l_{\rm p} = \frac{k^{\hat{t}}_{\rm (F)}}{k^{\hat{z}}_{\rm (F)}}\, H. \tag{13}$$

So far, we have discussed the emitted intensity in the fluid frame. This intensity is Doppler-boosted by a factor of $\delta^{3+\alpha_\nu}$ by the time it reaches the observer.[127] Thus, the intensity $|P|$ of linearly polarized synchrotron radiation that reaches the observer from the location P is

$$|P| = \delta^{3+\alpha_\nu}\, l_{\rm p}\, |\boldsymbol{B}|^{1+\alpha_\nu} \sin^{1+\alpha_\nu}\zeta \tag{14}$$

$$\rightarrow \delta^4\, l_{\rm p}\, |\boldsymbol{B}|^2 \sin^2\zeta \text{ for } \alpha_\nu = 1, \tag{15}$$

where we have omitted a proportionality constant. Since $|\boldsymbol{B}|$ is constant around the ring, the factors involving $|\boldsymbol{B}|$ could be eliminated from Equations (14) and (15) and absorbed into the omitted proportionality constant. We retain these factors because keeping track of $|\boldsymbol{B}|^2$ and its components is convenient for much of the analysis in Appendix D.[128]

2.3. Transformation of Polarization Vector

We next work on the polarization vector. In the fluid frame, the $\boldsymbol{E}$-vector of the radiation is oriented along $\boldsymbol{k}_{\rm (F)} \times \boldsymbol{B}$, i.e., perpendicular to both $\boldsymbol{k}_{\rm (F)}$ and $\boldsymbol{B}$. Therefore, we write the orthonormal components of the polarization 4-vector f^μ as

$$f^{\hat{t}}_{\rm (F)} = 0, \qquad f^{\hat{x}}_{\rm (F)} = \frac{(\boldsymbol{k}_{\rm (F)} \times \boldsymbol{B})_{\hat{x}}}{|\boldsymbol{k}_{\rm (F)}|},$$
$$f^{\hat{y}}_{\rm (F)} = \frac{(\boldsymbol{k}_{\rm (F)} \times \boldsymbol{B})_{\hat{y}}}{|\boldsymbol{k}_{\rm (F)}|}, \quad f^{\hat{z}}_{\rm (F)} = \frac{(\boldsymbol{k}_{\rm (F)} \times \boldsymbol{B})_{\hat{z}}}{|\boldsymbol{k}_{\rm (F)}|}. \tag{16}$$

By construction, this 4-vector satisfies

$$f^\mu k_\mu = 0, \qquad f^\mu f_\mu = \sin^2\zeta\, |\boldsymbol{B}|^2. \tag{17}$$

An inverse Lorentz boost transforms the 4-vector $f^{\hat{\mu}}_{\rm (F)}$ back to the P-frame:

$$\begin{aligned} f^{\hat{t}}_{\rm (P)} &= \gamma f^{\hat{t}}_{\rm (F)} + \gamma\beta\cos\chi\, f^{\hat{x}}_{\rm (F)} + \gamma\beta\sin\chi\, f^{\hat{y}}_{\rm (F)}, \\ f^{\hat{x}}_{\rm (P)} &= \gamma\beta\cos\chi\, f^{\hat{t}}_{\rm (F)} + (1 + (\gamma-1)\cos^2\chi) f^{\hat{x}}_{\rm (F)} \\ &\quad + (\gamma-1)\cos\chi\sin\chi\, f^{\hat{y}}_{\rm (F)}, \\ f^{\hat{y}}_{\rm (P)} &= \gamma\beta\sin\chi\, f^{\hat{t}}_{\rm (F)} + (\gamma-1)\cos\chi\sin\chi\, f^{\hat{x}}_{\rm (F)} \\ &\quad + (1 + (\gamma-1)\sin^2\chi) f^{\hat{y}}_{\rm (F)}, \\ f^{\hat{z}}_{\rm (P)} &= f^{\hat{z}}_{\rm (F)}. \end{aligned} \tag{18}$$

Since the Cartesian unit vectors $\hat{x}$, $\hat{y}$, $\hat{z}$ in the P-frame are oriented along the spherical polar unit vectors $\hat{r}$, $\hat{\phi}$, $-\hat{\theta}_{\rm o}$ of the Schwarzschild frame, the orthonormal components of k and f in Schwarzschild coordinates are

$$k^{\hat{t}} = k^{\hat{t}}_{\rm (P)}, \quad k^{\hat{r}} = k^{\hat{x}}_{\rm (P)}, \quad k^{\hat{\theta}} = -k^{\hat{z}}_{\rm (P)}, \quad k^{\hat{\phi}} = k^{\hat{y}}_{\rm (P)}, \tag{19}$$

$$f^{\hat{t}} = f^{\hat{t}}_{\rm (P)}, \quad f^{\hat{r}} = f^{\hat{x}}_{\rm (P)}, \quad f^{\hat{\theta}} = -f^{\hat{z}}_{\rm (P)}, \quad f^{\hat{\phi}} = f^{\hat{y}}_{\rm (P)}. \tag{20}$$

The photon geodesic emitted at P has three conserved quantities (see for instance Bardeen 1973): its energy $k_t = -1$, its angular momentum around the $\hat{z}$ axis $k_\phi = Rk^{\hat{\phi}}$, and the Carter (1968) constant C, which is the square of the total angular momentum of the photon for the Schwarzschild metric. In the P-frame the Carter constant is

$$C = R^2[(k^{\hat{\theta}})^2 + (k^{\hat{\phi}})^2]. \tag{21}$$

Using the conservation of k_ϕ and C, we find the coordinates x and y of the geodesic at the observer sky plane (recall the orientation of the sky coordinates x, y described at the top of Section 2) (Bardeen 1973),

$$\begin{aligned} x &= -\frac{k_\phi}{\sin\theta_{\rm o}} = -\frac{Rk^{\hat{\phi}}}{\sin\theta_{\rm o}}, \\ y &= k_\theta = R[(k^{\hat{\theta}})^2 - \cot^2\theta_{\rm o}(k^{\hat{\phi}})^2]^{1/2}\ \mathrm{sgn}(\sin\phi). \end{aligned} \tag{22}$$

To compute the polarization vector at the observer, we make use of the Walker–Penrose constant $K_1 + iK_2$ (Walker & Penrose 1970), which takes a simple form for a Schwarzschild spacetime. At the position P, we have (using the sign convention in Himwich et al. 2020),

$$K_1 = R(k^t f^r - k^r f^t), \qquad K_2 = -R^3(k^\phi f^\theta - k^\theta f^\phi). \tag{23}$$

Both K_1 and K_2 are conserved along the geodesic. Therefore, knowing their values, we can evaluate the two transverse components of the polarization electric field $\boldsymbol{E}$ at the observer. If we use the normalization used in Himwich et al. (2020), the field components are

$$\begin{aligned} E_{x,\rm norm} &= \frac{yK_2 + xK_1}{[(K_1^2 + K_2^2)(x^2+y^2)]^{1/2}}, \\ E_{y,\rm norm} &= \frac{yK_1 - xK_2}{[(K_1^2 + K_2^2)(x^2+y^2)]^{1/2}}, \\ E^2_{x,\rm norm} + E^2_{y,\rm norm} &= 1, \end{aligned} \tag{24}$$

[127] In the context of a continuous relativistic jet, a Doppler boost factor of $\delta^{2+\alpha_\nu}$ is generally used (e.g., Blandford & Königl 1979). That corresponds to the combined quantity $l_p\delta^{3+\alpha_\nu}$, where for motion parallel to the jet axis, $l_p \propto \delta^{-1}$. Our formulation, with l_p handled as a separate factor, is more general.

[128] Alternatively, we could assume $|\boldsymbol{B}| = 1$, as indeed we do in all the plots, eliminate $|\boldsymbol{B}|$ from Equations (14) and (15), but still keep track of the components of $\boldsymbol{B}$ in Appendix D.

which is normalized to unity. This normalization is suitable for plotting the orientation of polarization vectors in the xy-plane.

An alternative normalization is

$$E_x = \frac{yK_2 + xK_1}{x^2 + y^2},$$
$$E_y = \frac{yK_1 - xK_2}{x^2 + y^2},$$
$$E_x^2 + E_y^2 = \sin^2\zeta\ |\boldsymbol{B}|^2. \tag{25}$$

This retains the original normalization of f^μ in the fluid frame (Equation (17)), hence the electric field is proportional to $\sin\zeta\ |\boldsymbol{B}|$.

For computing the observed polarized intensity, we need to include the dependence on the Doppler factor δ and path length l_p, and must also ensure the correct powers of $\sin\zeta$ and $|\boldsymbol{B}|$ as given in Equations (14) and (15). Since the intensity is proportional to $|\boldsymbol{E}|^2$, we therefore write the observed electric field components as

$$\begin{aligned} E_{x,\rm obs} &= \delta^{(3+\alpha_\nu)/2}\ l_{\rm p}^{1/2} (\sin\zeta)^{(1+\alpha_\nu)/2}\ |\boldsymbol{B}|^{(1+\alpha_\nu)/2}\ E_{x,\rm norm} \\ &= \delta^{(3+\alpha_\nu)/2}\ l_{\rm p}^{1/2} (\sin\zeta)^{(\alpha_\nu-1)/2}\ |\boldsymbol{B}|^{(\alpha_\nu-1)/2}\ E_x, \end{aligned} \tag{26}$$

$$\begin{aligned} E_{y,\rm obs} &= \delta^{(3+\alpha_\nu)/2}\ l_{\rm p}^{1/2} (\sin\zeta)^{(1+\alpha_\nu)/2}\ |\boldsymbol{B}|^{(1+\alpha_\nu)/2}\ E_{y,\rm norm} \\ &= \delta^{(3+\alpha_\nu)/2}\ l_{\rm p}^{1/2} (\sin\zeta)^{(\alpha_\nu-1)/2}\ |\boldsymbol{B}|^{(\alpha_\nu-1)/2}\ E_y, \\ E_{x,\rm obs}^2 &+ E_{y,\rm obs}^2 = |P(\phi)|, \end{aligned} \tag{27}$$

where $P(\phi)$ is the observed linear polarized intensity of radiation that is originally emitted by a fluid element at ring azimuthal angle ϕ.

We need one more transformation: we must convert the coordinates $(R,\ \phi)$ of the emitting region in the fluid to the Cartesian sky coordinates $(x,\ y)$, or equivalently the polar sky coordinates $(\rho,\ \varphi)$, at which the radiation is observed,

$$x = \rho\cos\varphi, \quad y = \rho\sin\varphi. \tag{28}$$

The relation between $(R,\ \phi)$ and $(\rho,\ \varphi)$ is worked out in Appendix C. The observed linear polarization $P(\phi)$ can then be described in image coordinates by the complex function $P(\varphi)$,

$$P(\varphi) \equiv Q(\varphi) + iU(\varphi), \tag{29}$$

where the Stokes parameters $Q(\varphi)$ and $U(\varphi)$ are obtained from the electric field components $E_{x,\rm obs}$, $E_{y,\rm obs}$ using Equation (D10). The electric vector position angle (or EVPA) is then

$$\text{EVPA} \equiv \frac{1}{2}\arctan\frac{U}{Q}. \tag{30}$$

This completes the calculation of the intensities Q, U, P on the image plane. If one wishes to calculate fluxes in the sky plane corresponding to specific source configurations in ring coordinates $(R,\ \phi)$, it would be necessary to apply the Jacobian of the transformation from $(R,\ \phi)$ to $(\rho,\ \varphi)$, as in Figure 10. The Jacobian determinant is evaluated in Appendix C.

To summarize, in this section we showed how, given the position (R, ϕ, Figure 2) and velocity (β, χ, Equation (8)) of a synchrotron-emitting fluid element located on a tilted equatorial plane around a Schwarzschild black hole, and given also the magnetic field configuration ($B_{\rm eq}$, η, B_z, Equation (11)) in the frame of the fluid, one can calculate the sky coordinates (x, y, equivalently ρ, φ) of the image of this radiating element, and the linearly polarized intensity and position angle of the observed radiation. The mapping from the radiating element to the observer's image plane is written as a sequence of analytical calculations that do not require numerically integrating the geodesic equation or iteratively solving any equation. The equations are written in sufficient detail for easy incorporation into modeling calculations.

3. Example Models

The simple model considered in the previous section has the following parameters: tilt angle of the ring θ_o, ring radius R, velocity vector of the fluid $\boldsymbol{\beta}$, which is parameterized by $\beta = v/c$ and χ (Equation (8)), fluid frame magnetic field $\boldsymbol{B}$, which is parameterized by either B_r, B_ϕ, B_z, or $B_{\rm eq}$, η, B_z (Equation (11)), and spectral index α_ν. Figures 3–5 show the polarization patterns produced by this model for selected values of the parameters. In all these examples, we choose $\theta_o = 20^\circ$ and $\alpha_\nu = 1$.

Before considering the examples, we briefly summarize the salient features of the polarized image of M87* obtained by the EHT (EHTC VII). First, the linear polarized flux shows a pronounced asymmetry around the ring. The polarized flux is strong between PA (measured East of North) $\sim 150^\circ$ and $\sim 300^\circ$; the peak polarized intensity is around PA 200° on April 5 and 240° on April 11. The linear polarized flux is much weaker at other angles. The large scale jet in M87* is oriented toward PA 288°. Presumably, the accretion disk is also tilted toward this direction. Such a tilt is consistent with the EHT total intensity image shown in EHTC IV. Thus, if we measure angles counter-clockwise with respect to the presumed tilt direction in M87*, the polarized flux is strong between angles $\sim +10^\circ$ and -140°, with peak at -90° and -50° on April 5 and 11.

In our analytic model, the tilt and putative jet are toward the North. Thus, for a direct comparison of this model with the M87* image, we should rotate the calculated image clockwise by 72°. Alternatively, we could measure angles as offsets from the jet direction North. Thus, for a model to reproduce what is seen in M87*, it should have strong linearly polarized flux between $+10^\circ$ from the jet, i.e., just to the left of North, and -140° from the jet, which is located in the lower-right quadrant. That is, the polarized flux should concentrate in the right half of the panels in plots such as Figures 3–5 below, shading toward the upper right quadrant. As we will see, this is a fairly strong constraint.

The second piece of information from the polarized image of M87* is that the polarization vectors show a twisting pattern that wraps around the black hole (EHTC VII, VIII). The twist is described quantitatively by the β_2 mode of the azimuthal decomposition of polarization described in Palumbo et al. (2020). The amplitude of β_2 describes the degree to which the EVPA obeys rotational symmetry and scales linearly with fractional polarization, while the phase of β_2 describes the twist angle between the EVPA and the local radial unit vector on the image. In the M87* image, the twist angle is fairly stable in the regions where the polarized flux is strong. With respect to the local radial direction, the EVPA of the polarization vector is rotated clockwise by $\sim 70^\circ$. This too is a strong constraint on models, as discussed at length in EHTC VIII.

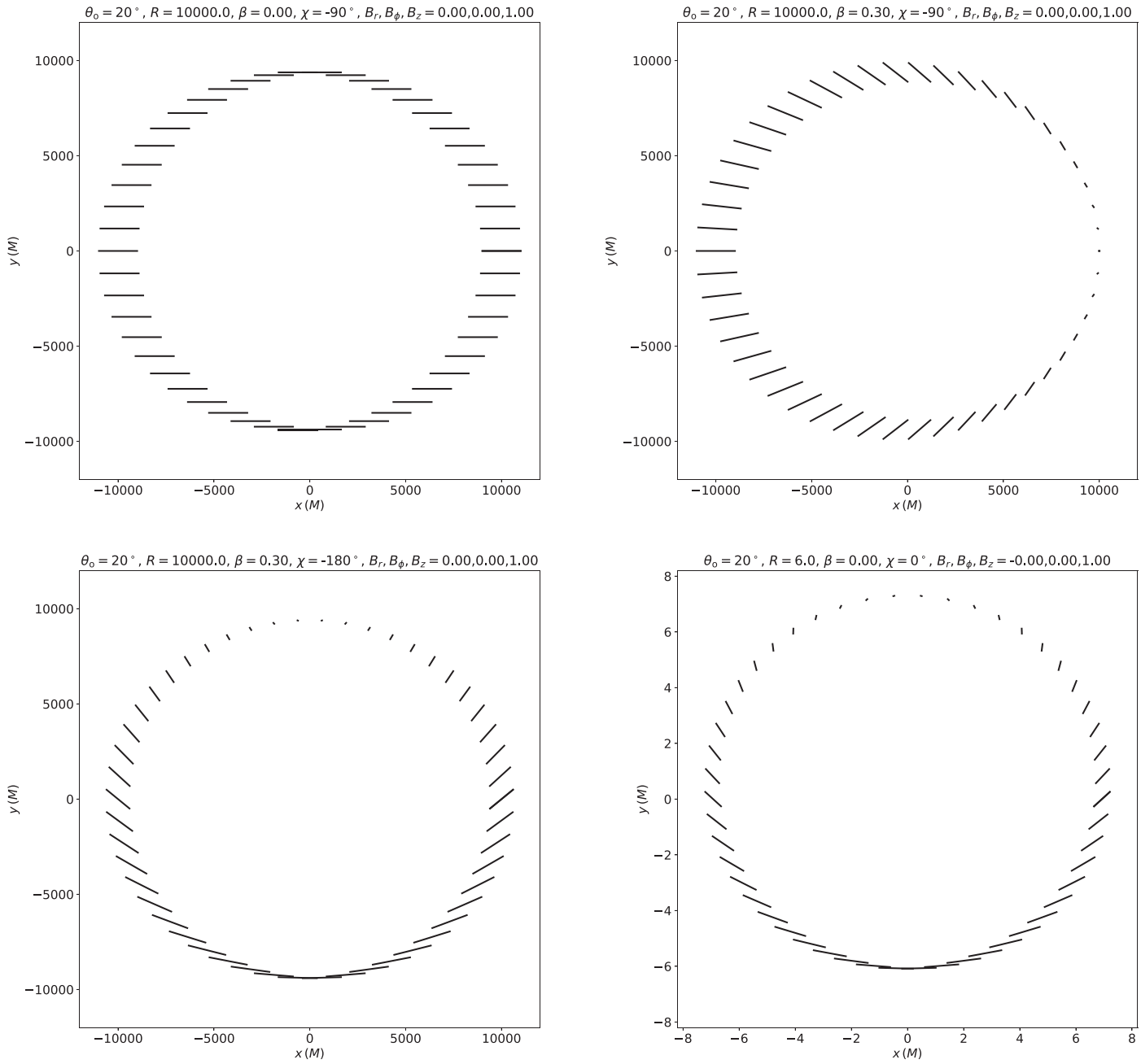

Figure 3. Polarization patterns corresponding to models with a "vertical" magnetic field (non-zero B_z in the fluid frame). In each case, the directions of the ticks indicate the orientation of the polarization $\boldsymbol{E}$-vector around the ring as viewed on the sky. The lengths of the ticks are proportional to the polarized intensity. Top left: ring with a very large radius and no orbital velocity, so that neither velocity aberration nor lensing plays a role. Top right: large ring radius (i.e., no lensing), and fluid orbiting with a tangential velocity $\beta = 0.3$ in the clockwise direction ($\chi = -90°$). Bottom left: large ring radius (no lensing), and fluid flowing with velocity $\beta = 0.3$ radially inward ($\chi = -180°$). Bottom right: ring with a small radius $R = 6M$, hence strong gravitational lensing, but with no fluid velocity, hence no aberration.

3.1. Models with Pure Vertical Field

Gravity Collaboration et al. (2018a) reported observations of polarized flares in Sgr A* in near-IR, and showed that a model with a dominant vertical magnetic field can reproduce the observations. Motivated by this, we begin by studying the predictions of our toy model for a pure vertical field, oriented normal to the plane of the emitting ring.

Figure 3 shows results from the analytical model for the case when $B_z = 1$, $B_r = B_\phi = 0$. It explores the two primary physical effects other than magnetic field direction that influence the observed polarization: (i) Doppler beaming and relativistic aberration caused by motion of the radiating fluid, and (ii) gravitational lensing caused by the gravity of the black hole. The top left panel in Figure 3 corresponds to a ring with a large radius ($R = 10^4$) such that there is negligible gravitational lensing. We also set $\beta = 0$, thereby eliminating Doppler beaming and aberration. The only remaining effect is the tilt of the ring, which causes the pure B_z field in the ring frame to appear in projection on the sky as a vertically oriented (north–south) field. The polarized synchrotron emission from the ring has its EVPA perpendicular to the projected field, i.e., in the east–west direction. The observed polarized intensity, which is indicated by the sizes of the polarization ticks in the plot, is uniform around the ring. In this figure and all others shown in

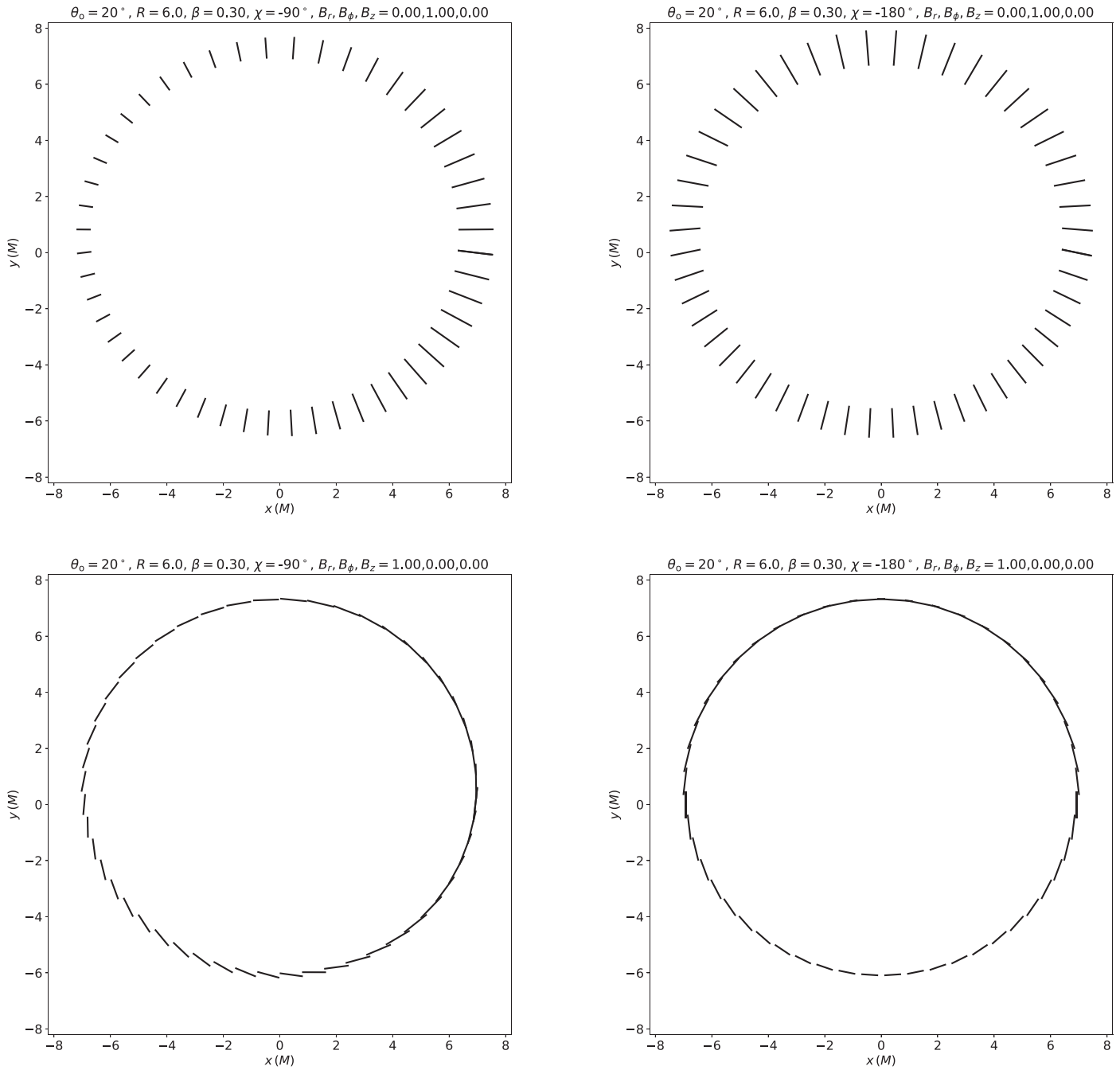

Figure 4. Polarization patterns for models with magnetic field in the equatorial plane. Top left: azimuthal field ($\eta = 90°$) with azimuthal clockwise velocity ($\chi = -90°$). Top right: azimuthal field ($\eta = 90°$) with radial inward velocity ($\chi = -180°$). Bottom left: radial field ($\eta = 0°$) with azimuthal clockwise velocity ($\chi = -90°$). Bottom right: radial field ($\eta = 0°$) with radial inward velocity ($\chi = -180°$).

this section, ticks are shown at 50 equally spaced positions in ϕ.

The top right panel in Figure 3 shows the effect of including an arbitrary relativistic velocity ($\beta = 0.3$) for the fluid in the clockwise tangential direction ($\chi = -90°$), but still keeping a large radius, hence no gravitational deflection. In this case, there is a strong asymmetry in the polarized flux around the ring. However, the bright region of the ring is in the left half of the plot, exactly the opposite of what we require to explain M87*. This contrary behavior is actually rather surprising. Given the direction of the tilt and the clockwise sense of rotation, the fluid in the right half of the plot has a component of its motion toward the observer, while the fluid on the left has a component away from the observer. Doppler beaming ought to favor the right side, yet we see the opposite. This paradoxical behavior is because of aberration, as we explain in Section 4.

The bottom left panel in Figure 3 shows the effect of a pure inward radial velocity ($\chi = -180°$), again for a large ring radius. Once again, the bright region of the disk is on the wrong side compared to what is seen in M87*. It is also exactly the opposite of what we would expect from Doppler beaming, since the fluid in the upper half has a velocity component toward the observer, and ought to be bright. Once again, aberration is the explanation.

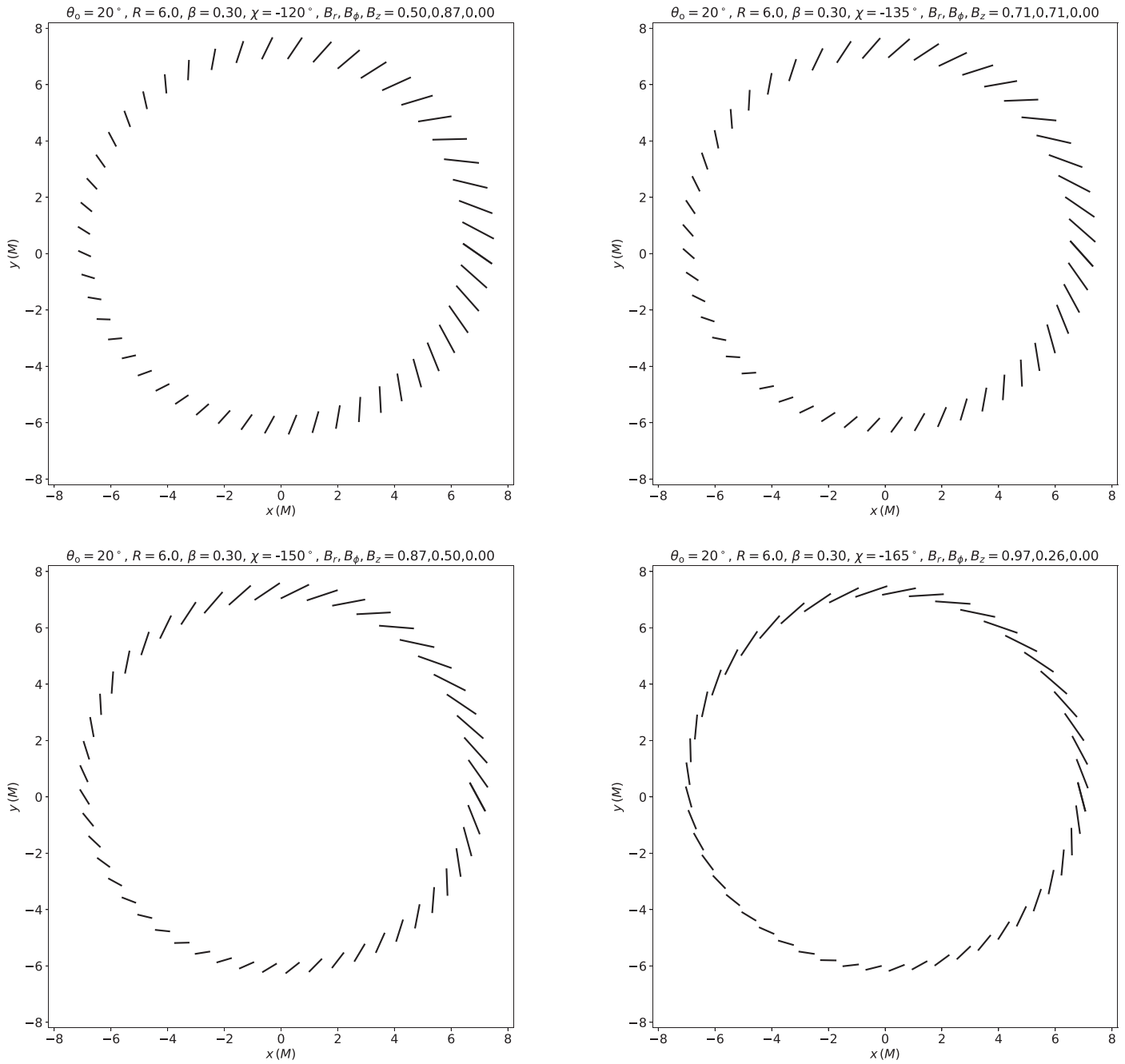

Figure 5. Polarization patterns for four models that include both radial and azimuthal components of velocity and magnetic field. The models correspond to $\chi = -120°$ (top left), $\chi = -135°$ (top right), $\chi = -150°$ (bottom left), $\chi = -165°$ (bottom right), each with magnetic field trailing opposite to the velocity ($\eta = \chi + 180°$). The two models in the bottom row come closest to reproducing the polarization pattern seen in M87*.

Finally, the bottom right panel considers a ring at small radius ($R = 6$) such that gravitational deflection of light rays is important. For simplicity, we assume that there is no fluid velocity. In this case, the results are similar to the bottom left panel, and the strongest polarized flux is at the bottom, which does not match what is seen in M87*.

We do not discuss the β_2 phase of the polarization patterns for models with pure vertical field, except to note that in the regions where M87* has its strongest polarized flux (upper right), the sense of the EVPA twist seen in all the examples in Figure 3 has the wrong sense.

The conclusion from these examples is the following. If the polarized emission that we see in M87* at 230 GHz is from equatorial gas, and if the gas rotates in the clockwise direction, as EHTC V concluded, and/or flows radially inward, as is natural for accretion, then the magnetic field cannot be dominated by a pure vertical component. There must be substantial radial and tangential field components.

Note that the observed ring in the bottom right panel in Figure 3 has a radius slightly larger than the original ring radius $R = 6$. The ring is also shifted slightly upward relative to the origin. Both effects are the result of gravitational deflection, as we explain in Section 4. The effect is seen only when R is small (gravity is strong), which is the case in this panel of Figure 3, and in all the panels in Figures 4, 5.

3.2. Models with Pure Radial or Tangential Field

We now turn our attention to models with magnetic field entirely in the equatorial plane, i.e., $B_z = 0$, non-zero B_r or B_ϕ. We consider a ring with small radius ($R = 6$) and include relativistic fluid motion; thus, lensing, Doppler and aberration are all included. Figure 4 shows four models, two with radial field ($\eta = 0°$) and two with tangential field ($\eta = 90°$). For each field configuration, we consider two velocity fields, either pure clockwise rotation ($\chi = -90°$) or pure radial infall ($\chi = -180°$).

Three of the four panels in Figure 4 have their strongest polarized flux in the correct region of the ring (top and/or right) to match what is seen in M87*. Even the fourth (top right panel) has slightly stronger polarized flux at the top. The very different behavior of these models, compared to those in Figure 3, is explained in detail in the next section. In brief, for models with magnetic field restricted to the equatorial plane, aberration induces the same sense of flux asymmetry as Doppler beaming and therefore enhances the effect of the latter, whereas in the pure B_z models, aberration induces flux asymmetry with the opposite sign of that due to Doppler beaming, and in fact overwhelms the latter and reverses the sign of what is observed. In this sense, equatorial field-dominated models are more promising for M87*.

Considering the twist of the polarization pattern, as discussed in EHTC VIII, a pure tangential field is ruled out because the polarization ticks are predicted to be purely radial, which does not match M87. A pure radial field is also ruled out since it predicts polarization ticks entirely in the tangential direction. However, these models come closer to what is seen in M87*. It would appear that models in which $B_r > B_\phi$ are most suitable.

3.3. Models with Both Radial and Tangential Field

Figure 5 shows four models in which both B_r and B_ϕ are non-zero, and $B_z = 0$. All the models have fluid with clockwise rotation in the sky and radial infall, i.e., the angle χ of the vector $\boldsymbol{\beta}$ is in the lower left quadrant. Since the radial and tangential magnetic field components in the inner regions of an accretion disk are likely oriented parallel to the motion of the fluid—the field is "combed out" by the flow—we simplify matters by assuming that the field is aligned with the velocity. Specifically, we choose

$$\text{Pure } B_{\rm eq}: \quad \eta = \chi \text{ or } \eta = \chi + \pi. \tag{31}$$

For the specific case of a purely equatorial field, we can choose either of the two values of η indicated above. The two choices correspond to oppositely oriented directions of the magnetic field lines; this ambiguity has no effect on the linear polarized emission. As we discuss in Section 3.5, we need to be more careful about the choice of η when we have both vertical and equatorial field components.

In Figure 5, the model in the top left panel has tangential velocity larger than radial velocity, and correspondingly $B_\phi > B_r$. In the top right panel, the radial and tangential components are equal, while in the lower two panels the radial components of velocity and magnetic field are larger than the respective tangential components. All four models have flux asymmetry that qualitatively matches M87*. All four models also have polarization patterns with the same sense of twist, or sign of β_2 phase, as observed in M87*. Among the four models, the ones in the bottom row come closest to M87*.

3.4. Models with R = 4.5 M and Varying Inclination

We round out the discussion of examples by considering models with a smaller emission radius, $R = 4.5$, which is better matched to M87*, and exploring the effect of varying the tilt angle θ_o. Figure 6 shows models with $\chi = -150°$, $\eta = \chi + \pi = 30°$, and four choices of θ_o: 20°, 40°, 60°, and 80°.

The top left panel has $\theta_o = 20°$ and is designed to resemble M87*. The polarized intensity asymmetry (relative to the direction of the jet), as well as the twist of the EVPA pattern, are similar to the EHT observations described in EHTC VII and EHTC VIII. This same model is shown again in Figure 9 with the polarization pattern rotated counter-clockwise by 288° to match the jet orientation in M87*, and with the emitting fluid spread out in radius with an exponential profile with scale width $2M$ (see Section 5.1 for details), instead of the infinitely thin emitting ring assumed here.

The remaining panels in Figure 6 show the effect of increasing the tilt angle θ_o. The Doppler asymmetry in the polarized intensity increases rapidly since the fluid motion has a larger component parallel to the line of sight. The orientation of the asymmetry (bright on the right, dim on the left) as well as the twist of the polarization pattern qualitatively resemble what is seen in the $\theta_o = 20°$ model. The ring appears increasingly flattened as θ_o increases, but it also acquires an additional asymmetry such that, by $\theta_o = 80°$ it looks more like a semi-circle than an ellipse. This is because of extreme lensing of radiation emitted from the far side of the ring. As in the previous figures, ticks are equally spaced in ϕ; the large gaps on the north side of the $\theta = 80°$ image indicate the relative stretching between φ and ϕ at high inclination.

3.5. Models with All Field Components

We finally discuss models in which all three components of the magnetic field are non-zero. In this general case, we need to be careful about the geometry of the magnetic field. In a three-dimensional accretion flow in which magnetic field lines penetrate the disk from one side to the other, as for instance in a magnetically arrested disk (MAD) field geometry (Igumenshchev et al. 2003; Narayan et al. 2003; Tchekhovskoy et al. 2011; Bisnovatyi-Kogan 2019), one expects a reflection antisymmetry in $B_{\rm eq}$ about the midplane. That is, B_r and B_ϕ would flip sign when crossing the mid-plane, whereas B_z would retain the same sign on the two sides. Let us assume, without loss of generality, that B_z is positive, i.e., the z-component of the magnetic field line is pointed toward the observer, and let us also take $B_{\rm eq}$ to be positive. If the magnetic field is dragged and aligned with the flow, as we assumed in the previous two subsections, the field angle η and the flow velocity angle χ must be related as follows on the two sides of the disk,

$$\begin{aligned} z > 0 \text{ (near side)}: &\quad \eta = \chi + \pi, \\ z < 0 \text{ (far side)}: &\quad \eta = \chi, \end{aligned} \tag{32}$$

where "near side" means the side of the disk facing the observer.

In the absence of Faraday rotation effects, the above antisymmetry affects emission only by changing the relative

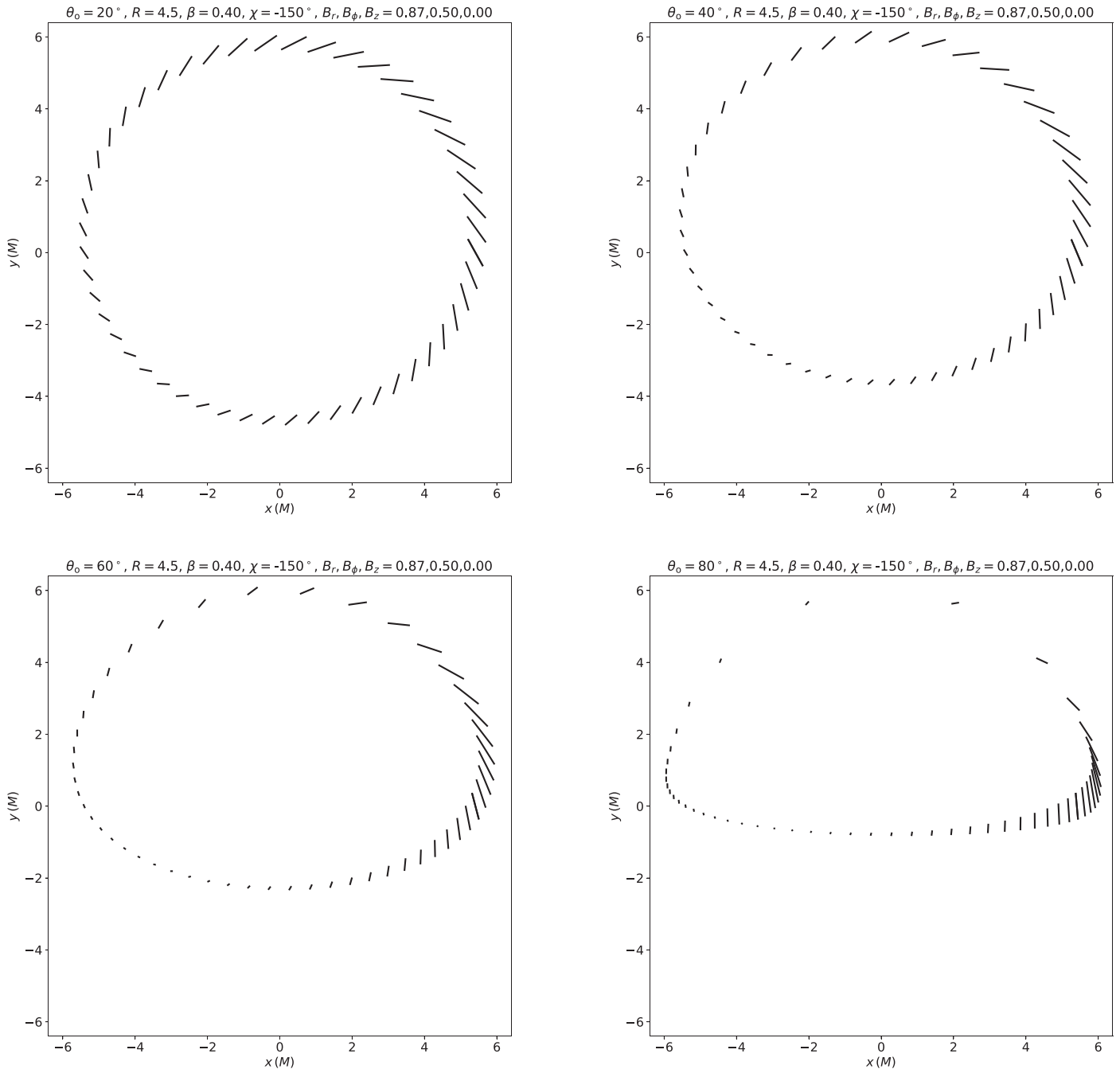

Figure 6. Polarization patterns for four models with equatorial magnetic field and emission radius $R = 4.5$, viewed at different inclination angles. Top left: $\theta_o = 20°$. Top right: $\theta_o = 40°$. Bottom left: $\theta_o = 60°$. Bottom right: $\theta_o = 80°$. All the models have velocity angle $\chi = -150°$, and magnetic field trailing opposite to the velocity ($\eta = \chi + 180°$). The model in the top left, rotated counter-clockwise by 288° and with emission spread over a finite range of radii, is shown in Figure 9 as a toy model of M87*.

sign between B_{eq} and B_z, hence it is not relevant if either B_{eq} or B_z is zero. However, when both B_{eq} and B_z are non-zero, one should separately compute the polarized image produced by the near side and far side of the disk and add the resulting Stokes parameters.

If Faraday effects internal to the flow are strong enough to depolarize the emission from the far side, the polarized image seen by the observer will be dominated by the near side. The simulations considered in EHTC VIII, for instance, generally show large internal Faraday depths. In such cases, we need compute only a single image from the near side of the disk, setting $\eta = \chi + \pi$.

We do not show examples of models with both vertical and equatorial field since the parameter space is large.

3.6. Numerical Geodesics and Effect of Spin

A general Beloborodov-like analytic approximation for the emission angle of photons from equatorial matter around a spinning black hole is not known. However, it is possible to solve analytically for the observed polarization once the photon's arrival coordinates on the image are determined from a numerical solution to the geodesic equation; this relation can be explicitly expressed in terms of real elliptic integrals

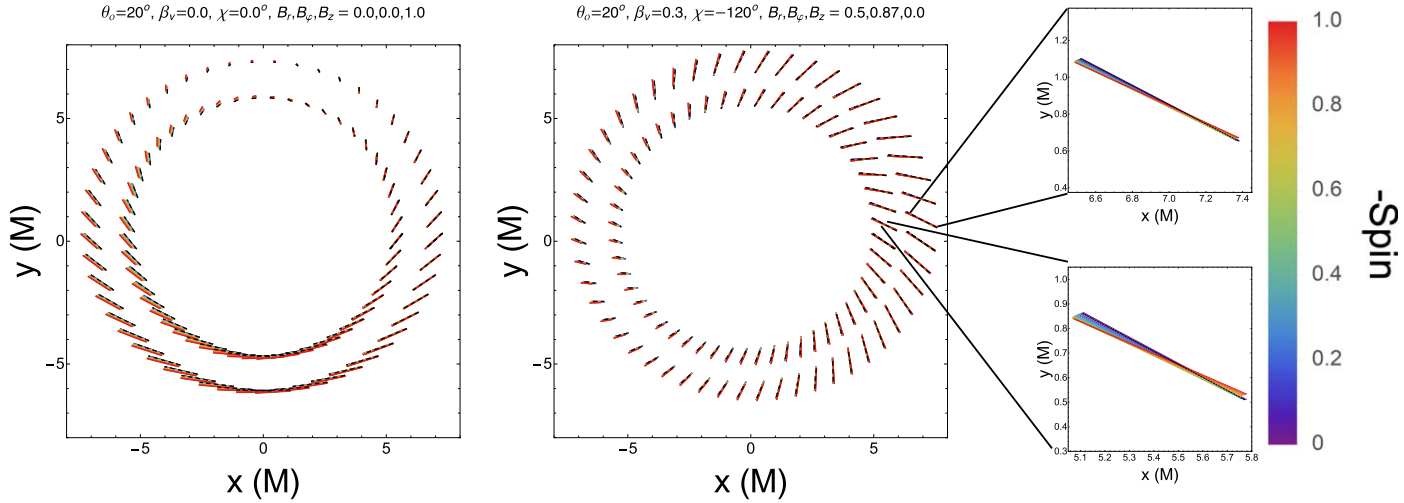

Figure 7. The effects of spin on the observed polarization pattern. Each of the two main panels displays a different configuration of magnetized fluid. The first panel corresponds to the bottom right panel of Figure 3 and the second panel corresponds to the top left panel of Figure 5. Both panels show an inclination of 20° and negative spin (i.e., clockwise rotation on the image). The inner and outer rings of polarization ticks correspond to emission from $R = 4.5$ and $R = 6$, respectively. The color bar shows increasing spin from $a = 0$ to $|a| = 1$, and the Beloborodov approximation for Schwarzschild is shown in black overlaid dashes. The two small panels display a zoom-in of one set of ticks at $R = 4.5$ (lower) and $R = 6$ (upper).

(Gralla & Lupsasca 2020a, 2020b, see also Li et al. 2005; Gates et al. 2020 for a calculation of images of an orbiting emitter in this formalism). For a spinning black hole, we generalize the P-frame to the "zero-angular-momentum-observer" (ZAMO) frame, and then consider a boost $\boldsymbol{\beta}$ as in (8) into the corresponding F-frame. The semi-analytic result for the polarized image of such a boosted fluid orbiting a spinning black hole is presented in Figure 7, in which changing spin is plotted by color. The inner and outer ring in the first two panels correspond to emission radii of $R = 4.5$ and $R = 6$, respectively. The results of the Beloborodov approximation are overlaid with black dashed lines and coincide with the low spin semianalytic solution from Kerr. The first and second panels of Figure 7 generalize the scenarios from the bottom right panel of Figure 3 and the upper left panel of Figure 5, respectively. The small panels zoom in on one set of ticks from the second panel.

Figure 7 illustrates that for the idealized case of purely geometric and relativistic effects that we consider here, black hole spin has only a small effect on the observed EVPA and can be reasonably neglected for the purposes of the toy model. It also shows that the Beloborov approximation is fairly accurate even at radii as small as $R = 4.5$. The effects of spin on observed polarization become more pronounced at very small radius and high observer inclination, neither of which are considered in this paper but will be the subject of future work.

3.7. Generalizations

Although the examples presented in this paper are restricted to axisymmetric models with emission limited to a single radius, the underlying model is more general. The primary result of the analysis presented in Section 2 is an analytical method to map emission properties at a given (R, ϕ) in the emitting ring to the properties of the observed radiation in the sky plane. This transformation can be easily applied to models with non-axisymmetric emission, as well as to radially extended sources. In such models, $|\boldsymbol{B}|$ would be a function of location and this would need to be included in the calculations. Other quantities like the electron temperature and number density that affect the emissivity could also vary with position and will need to be accounted for.

Two other approximations in the model, both made in the interests of simplicity, deserve discussion: (1) We restricted the emitting gas to lie in a single equatorial plane. (2) We took the velocity to lie entirely within the same plane (though we did allow for a general magnetic field). Both limitations can be eliminated.

The Beloborodov approximation can be applied at any emission location (R, ϕ, z), not just at equatorial locations. For non-equatorial locations, the geometry of the Geodesic Frame and the computation of α (Figure 1) will differ. This will modify the result for the components of $k^{\hat{\imath}}_{(\mathrm{P})}$. If a given null geodesic has contributions from several emission regions at different heights z from the equatorial plane, one could compute their individual contributions to the Stokes parameters and add the contributions incoherently.

Similarly, an off-plane velocity component will modify the Lorentz transformation coefficients between the P-Frame and the F-Frame, and will alter the geometrical factor that enters the path length calculation. The distinction between "vertical" and "in-plane" magnetic field components would become less clear, but this is merely a matter of definition.

The model discussed in this paper has been derived for a non-spinning (Schwarzschild) black hole. However, as shown in Section 3.6, and as discussed also in Gravity Collaboration et al. (2020) and EHTC VIII, black hole spin has very little effect on the polarized image, at least for the low inclination angles considered so far.

Finally, the analysis here is focused on optically thin synchrotron emission for which the polarization four-vector f^μ is given by Equation (16) and the electric field is normalized as in Equation (25). For optically thick emission from a thin accretion disk, other prescriptions will need to be substituted, e.g., Li et al. (2009) discuss polarization of X-rays emitted by the scattering atmosphere above a black hole X-ray binary disk. Except for this change, the rest of the analysis should remain the same.

4. Analytical Understanding of the Results

By Taylor-expanding the expressions given in Section 2 in suitably chosen "small" quantities, and keeping terms up to second order, we can obtain useful analytical approximations for various observables. This provides a physical understanding of the results shown in Section 3.

In the present context of trying to understand M87* and Sgr A*, we have three small quantities, $2/R \approx 1/3$ (lensing), $\beta \approx 1/3$ (Doppler and aberration), $\sin\theta_o \approx 1/3$ (ring tilt[129]), where the numerical values correspond to the models shown in Section 3. We treat all three quantities on an equal footing in the series expansions we carry out. The full results, with all terms up to quadratic order, are listed in Appendix D. The reason for going up to quadratic order is explained below. Here we use the series expansion of the equations to interpret the numerical results presented in Section 3.

4.1. Shape of the Observed Ring

We begin with the shape of the ring as observed on the sky. To quadratic order, the result is

$$x = (R+1)\cos\varphi + \left[-\frac{1}{2R}\cos\varphi + \sin\theta_o \sin 2\varphi - \frac{R}{2}\sin^2\theta_o \sin^2\varphi\cos\varphi\right], \quad (33)$$

$$y = (R+1)\sin\varphi + \left[-\frac{1}{2R}\sin\varphi + 2\sin\theta_o \sin^2\varphi - \frac{R}{2}\sin^2\theta_o \sin^3\varphi\right]. \quad (34)$$

The first term in each expression gives the answer up to linear order, and the remaining terms inside the square brackets correspond to quadratic order. Up to linear order we see that the observed ring is circular, but with an apparent radius larger by unity (i.e., GM/c^2) than the radius of the source ring. The radial "expansion" of the observed ring is caused by gravitational deflection (lensing) of geodesics. As shown in Figure 1, lensing causes the geodesic to curve around the black hole such that the impact parameter is larger than the naive straight-line estimate $R\sin\psi$.

Among the quadratic terms in Equations (33) and (34), the terms proportional to $1/R$ are second-order corrections to the ring radius, and the $\sin^2\theta_o$ terms describe the flattening of the observed ring because of tilt. The latter is simple geometry: a tilted circular ring appears elliptical in shape, with a minor axis radius equal to $\cos\theta_o \approx 1 - (1/2)\sin^2\theta_o$ times the original ring radius. The $\sin\theta_o$ terms describe the effect of tilt on lensing. Geodesics reaching the observer from the upper half of the ring ($0 < \phi < \pi$) travel a longer distance near the black hole and suffer more deflection (this is the case shown schematically in Figure 1), while geodesics from the lower half ($\pi < \phi < 2\pi$) experience less deflection. This causes an upward shift of the observed ring, i.e., a net positive bias in y. The shift is of the order of $\sin\theta_o$ in units of GM/c^2. The shift is seen in all the models in Section 3 that have a smallish radius ($R = 6$, lower right panel in Figure 3, and all panels in Figures 4–6).

[129] In the case of M87*, observations of the radio jet suggest a tilt $\theta_o \sim 17°$ (Walker et al. 2018), and in the case of Sgr A*, Gravity Collaboration et al. (2018a) estimate $\theta_o < 30°$ based on the polarization signatures of infrared flares.

4.2. Doppler Factor and sinζ

Expanding up to second order, we find for the Doppler factor δ,

$$\delta = \left(1 - \frac{1}{R}\right) - \left[\frac{\beta^2}{2} + \frac{1}{2R^2} - \frac{2\beta}{R}\cos\chi + \beta\sin\theta_o \sin(\chi+\varphi)\right], \quad (35)$$

where the second order terms are shown on the second line inside square brackets. The linear order term $-1/R$ describes deboosting of the observed intensity by gravitational redshift, and the first three second-order terms describe various other deboosting effects such as second-order Doppler. Since $\cos\chi$ is negative for radial infall, all three terms have a positive magnitude for the inflowing models we have considered, causing uniform dimming all around the ring.

Azimuthal modulation of the intensity from relativistic beaming is described by the final term, $\beta\sin\theta_o\sin(\chi+\varphi)$, and this is the only term that varies as a function of φ. The fact that this important effect appears only at second order is a major reason for expanding the equations up to quadratic order rather than stopping at linear. Why is it second order? It is because azimuthal modulation from Doppler beaming requires both tilt and fluid velocity, each of which is treated as a small quantity in our analysis.[130]

Doppler beaming causes an increase in the observed polarized intensity when $\sin(\chi+\varphi)$ is negative, with the maximum boost occurring when $\chi + \varphi = -90°$. For pure clockwise rotation ($\chi = -90°$), the maximum boost is at $\varphi = 0$. This is natural since, for a ring tilted toward the North, the fluid at $\varphi = 0$ has the largest velocity component toward the observer and hence produces the most Doppler-boosted radiation. For pure radial infall ($\chi = -180°$), the maximum boost is at $\varphi = 90°$, again because the fluid there has the maximum velocity toward the observer. Since we consider models that lie between these two extremes, we expect the polarized intensity to be maximum somewhere in the top right quadrant, $0 < \varphi < 90°$ (for a tilt to the North). This agrees with what is observed in M87* (once we allow for the different tilt/jet direction). Surprisingly, it is not true for the models shown in Figure 3. To understand the reason for this discrepancy, we need to consider a second effect.

From Equation (15), the observed polarized intensity depends on the Doppler factor δ as well as the path length l_p and the angle ζ between the photon wavevector $\boldsymbol{k}_{(F)}$ in the fluid frame and the local magnetic field $\boldsymbol{B}$. For small tilt angles, the variation in the path length is small and not very important. We ignore it in the discussion below. The angle ζ, however, is crucial since synchrotron emission is maximum when $\boldsymbol{k}_{(F)}$ and $\boldsymbol{B}$ are orthogonal to each other ($\zeta = \pm\,\pi/2$) and vanishes when they are parallel ($\zeta = 0,\ \pi$). Appendix D evaluates $|\boldsymbol{B}|^2\sin^2\zeta$ up

[130] For the models considered in Section 3, where each of the three small quantities is $\approx 1/3$, one expects second-order terms to be of order 10% of the leading-order terms. However, many second-order terms come with large coefficients, e.g., intensity is proportional to δ^4 so Doppler boost goes like $-4\beta\sin\theta_o\sin(\chi+\varphi)$. Hence the second-order contributions are often not small. The analysis in this section should thus be used only for qualitative understanding. For accurate results, it is necessary to evaluate numerically the full equations given in Section 2.

to quadratic order. We consider in the following subsections the effect of various terms in the series expansion.

4.3. Models with Pure Vertical Field

We begin by considering a model with pure B_z and consider the non-zero terms in $|\boldsymbol{B}|^2 \sin^2\zeta$:

$$B_z \text{ Finite, } B_{\rm eq} = 0:$$
$$|\boldsymbol{B}|^2 \sin^2\zeta = \left[-\frac{4}{R}\sin\theta_{\rm o}\sin\varphi + \frac{4}{R^2} + \sin^2\theta_{\rm o} - \frac{4\beta}{R}\cos\chi + 2\beta\sin\theta_{\rm o}\sin(\chi+\varphi) + \beta^2\cdots \right] B_z^2. \tag{36}$$

There are several interesting effects here. First, we have only second-order terms, no zeroth- or first-order terms (this is another reason for going up to second order in the analysis). It suggests that the observed flux should be strongly suppressed. This is not surprising since the emission toward the observer goes as $\sin^2\zeta \sim \sin^2\theta_{\rm o}$, which is small for models with small tilt. The lack of zeroth- and first-order terms also means that the importance of the second-order quantities in Equation (36) is enhanced.

Consider first the term $-(4/R)\sin\theta_{\rm o}\sin\varphi$, which describes the combined effect of lensing $(4/R)$ and tilt $(\sin\theta_{\rm o})$. Figure 1 shows the origin of this term. In the absence of lensing, a geodesic travels on a straight line to the observer and hence subtends an angle $\theta_{\rm o}$ to the (vertical) magnetic field. When gravitational ray deflection is included, the angle at the emission point is modified. For a point on the North or upper half of the ring (the case shown in Figure 1), the deflection is such that the photon wavevector becomes more nearly parallel to the z-axis, i.e., more parallel to the magnetic field. Thus ζ is reduced, and this causes the emissivity to go down. The decrease is largest when $\varphi = 90°$, as indeed we find in Equation (36). If we consider instead a point on the South or lower half of the ring, e.g., $\varphi = -90°$, the gravitational deflection works in the opposite sense and causes ζ to increase, and the emissivity to correspondingly increase. The net result is an asymmetry in the polarized flux around the ring such that the maximum flux is in the South and the minimum is in the North, precisely as seen in the bottom right panel in Figure 3.

Consider next the term $2\beta\sin\theta_{\rm o}\sin(\chi+\varphi)$, which corresponds to the combined effect of tilt and relativistic motion. Here the relevant effect is aberration. Because of the motion of the fluid, the orientation of the wavevector $\boldsymbol{k}_{\rm (F)}$ in the fluid frame is different from its orientation $\boldsymbol{k}_{\rm (P)}$ in the P-frame. The aberration effect is such that fluid that is moving toward the observer has $\boldsymbol{k}_{\rm (F)}$ rotated closer to the z-axis in the fluid frame, i.e., more nearly parallel to $\boldsymbol{B}$, while fluid that is moving away from the observer has the tilt of $\boldsymbol{k}_{\rm (F)}$ with respect to $\boldsymbol{B}$ increased. The former fluid element thus emits less and the latter more in the direction of the observer. This cancels the effect of Doppler beaming. Actually, since the constant φ-independent terms in Equation (36) are of the same order as the modulation term $\sin(\chi+\varphi)$ (note that $2\beta\sin\theta_{\rm o}$ is almost equal to $4/R^2 + \sin^2\theta_{\rm o} + \beta^2$), the cancellation tends to be quite pronounced when $\chi+\varphi \sim -90°$. The net effect is that aberration overwhelms Doppler beaming and gives the patterns seen in the top right and bottom left panels in Figure 3.

4.4. Models with Pure Equatorial Field

When we consider models with pure equatorial field ($B_{\rm eq}$ finite, $B_z = 0$), the situation is quite different. Focusing on $|\boldsymbol{B}|^2\sin^2\zeta$, we find

$$B_{\rm eq} \text{ Finite, } B_z = 0, \ \eta = \chi + \pi:$$
$$|\boldsymbol{B}|^2\sin^2\zeta \approx B_{\rm eq}^2 + [-2\beta\sin\theta_{\rm o}\sin(\chi+\varphi)\cdots]\, B_{\rm eq}^2, \tag{37}$$

where we have written only one of the second-order terms. As in Section 3, we have simplified matters by assuming that the magnetic field is oriented anti-parallel with the velocity: $\eta = \chi + \pi$.

The first thing to note is that in the case of an equatorial field there is a non-vanishing zero-order term. For small tilt, a magnetic field in the equatorial plane is almost orthogonal to the photon wavevector, hence synchrotron emissivity in the direction of the observer is nearly maximum. Correspondingly, the second-order terms are less important. Moreover, the second order term in Equation (37) appears with the same sign as the corresponding term in δ (Equation (35)), and the opposite sign as in Equation (36). The reason is simple. When aberration tilts the wavevector closer to the z-axis, the wavevector becomes more nearly orthogonal to $\boldsymbol{B}$, and hence the emissivity increases. Thus in equatorial field models, the second-order terms in $|\boldsymbol{B}|^2\sin^2\zeta$ cooperate with and enhance the effect of Doppler beaming, as seen in the panels in Figures 4 and 5. As an aside, when both $B_{\rm eq}$ and B_z are non-zero, and if we assume as before that $\eta = \chi + \pi$, then there is a first order term $-2\sin\theta_{\rm o}\sin(\eta+\varphi)B_{\rm eq}B_z$, which again has the same sign as the corresponding term in δ.

4.5. Twist of the Polarization Pattern

We now briefly discuss the twist of the polarization pattern around the ring. When the field is purely in the equatorial plane, the results are transparent. To zeroth order, the electric field in the sky plane is given by

$$E_{x,\rm obs} = -\sin\varphi\, B_r - \cos\varphi\, B_\phi = -\sin(\eta+\varphi)B_{\rm eq}^2,$$
$$E_{y,\rm obs} = \cos\varphi\, B_r - \sin\varphi\, B_\phi = \cos(\eta+\varphi)B_{\rm eq}^2. \tag{38}$$

That is, the electric field is oriented perpendicular to the projected magnetic field, as one would expect.

Instead of considering the electric field, one could consider the Stokes parameters Q and U and look at their Fourier coefficients β_m (Palumbo et al. 2020), as described in Appendix D. The most useful coefficient is β_2, whose complex phase directly gives the orientation of the twist. If the electric field is radial, the phase of β_2 is zero, if it is rotated clockwise from radial by 45°, the phase is −90°, and if the electric field is tangential, the phase is −180°. The EHT observations of M87* give a phase $\sim -130° \equiv +230°$. From Appendix D, the leading order term in β_2 in the case of a pure equatorial magnetic field is

$$\beta_2 \approx e^{i(\pi+2\eta)}B_{\rm eq}^2. \tag{39}$$

The phase of this quantity will match the phase observed in M87* if $\eta \sim 25°$. Hence, the magnetic field must be mostly radial.

When $B_{\rm eq} = 0$ and we have a purely vertical field, the phase of β_2 is determined by the coefficient of B_z^2, which consists

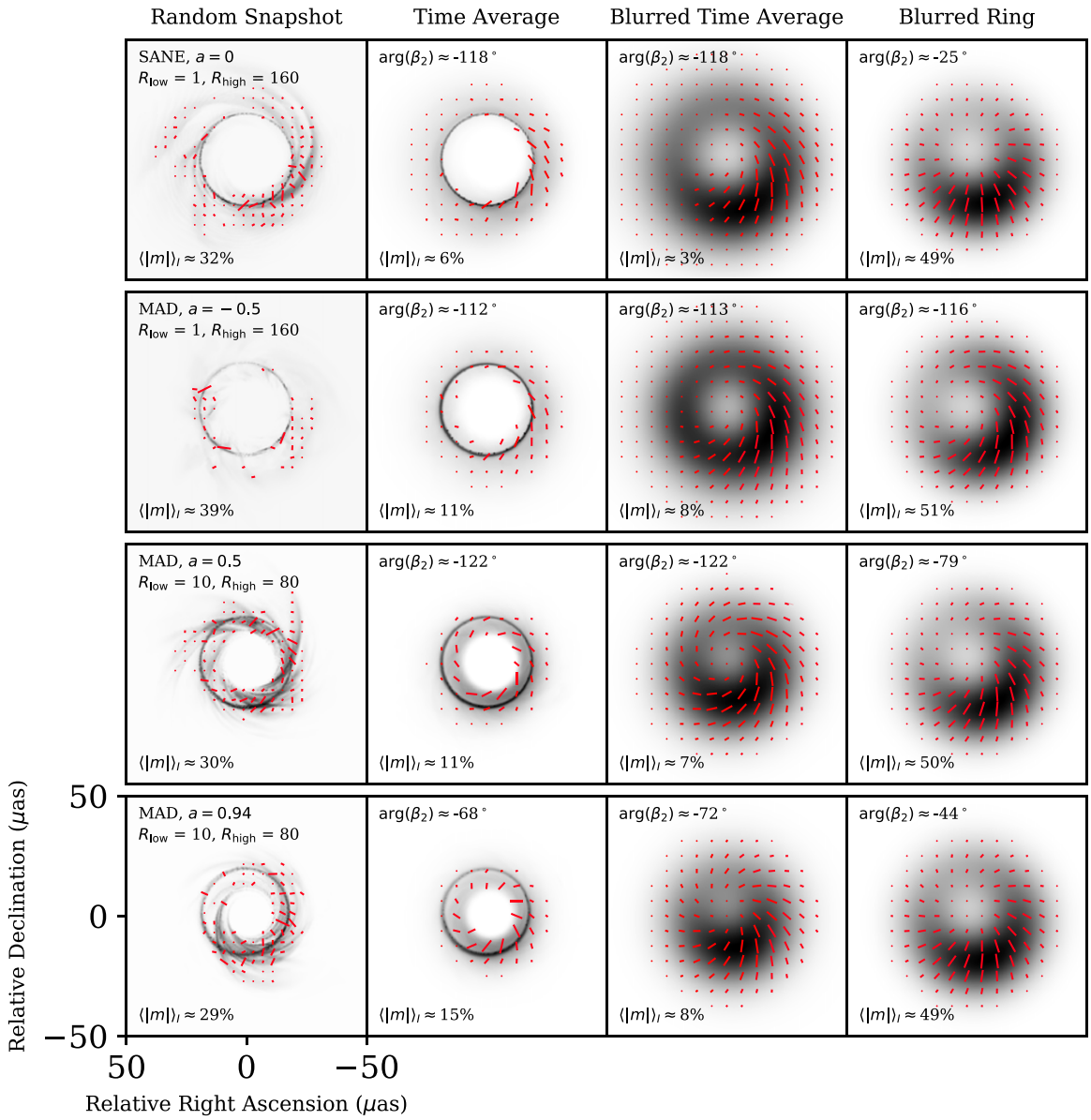

Figure 8. Comparison of GRMHD simulations to images of the ring model for simulation parameters favored in EHTC VIII. The left three columns show random snapshots, time averaged images, and blurred time averages of each GRMHD simulation; the right column shows the image generated by the simple ring model when evaluated for magnetic field and fluid velocity values taken from the simulations at $R = 4.5$ after azimuthal and temporal averaging. Ticks show polarization magnitude and position angle where total intensity exceeds 5% of the maximum. Grayscale shows total intensity in linear scale (directly proportional to polarization magnitude for the ring model). The total intensity and polarization magnitude are separately normalized in each panel. Panels show the average fractional polarization weighted by total intensity at bottom left; note that the GRMHD images are heavily depolarized, whereas the ring model images are not. The ring model and averaged images show the argument of the β_2 PWP mode at top left.

entirely of second-order terms:

$$B_{\rm eq} = 0: \quad \beta_2 = \left[\left(-\frac{4}{R^2} + \frac{4\beta}{R}e^{i\chi} - \beta^2 e^{2i\chi}\right)B_z^2\right]. \qquad (40)$$

If lensing is unimportant, i.e., R is large, then β^2 dominates and the phase of β_2 is determined by the orientation angle χ of the fluid velocity. For a radial velocity ($\chi = \pi$), the phase of β_2 is π, i.e., the polarization vectors should be tangentially oriented. This is indeed seen in the brightest part of the ring in the bottom left panel in Figure 3. Similarly, for a tangential velocity ($\chi = -\pi/2$), the phase of $\beta_2 = 0$ and the polarization ticks should be radial, as seen in the top right panel of Figure 3. Finally, if there is no velocity but we consider strong lensing (small R), then Equation (40) shows that β_2 has phase $= \pi$ and the polarization should be tangential, as in the bottom right panel.

5. Comparison to Observations

Our ring model provides a convenient framework for direct comparison with a variety of polarimetric observations of near-horizon emission. We now discuss two specific cases of particular interest: polarimetric imaging with the EHT and infrared flares of Sgr A*.

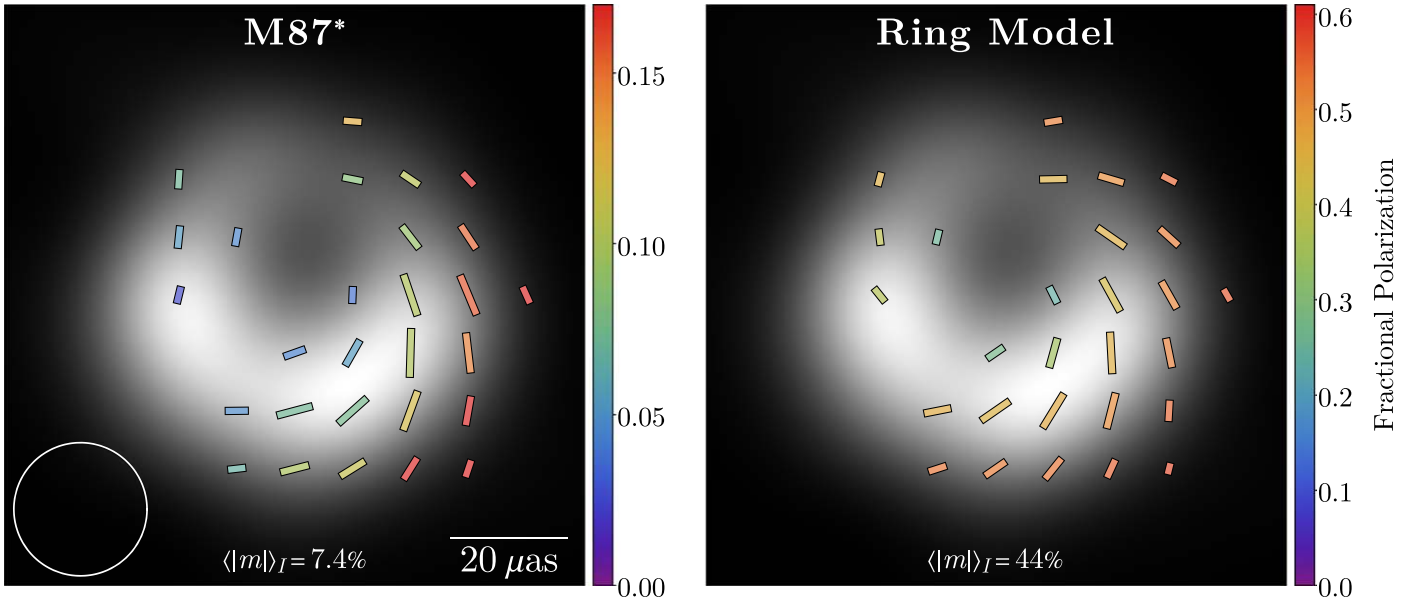

Figure 9. Comparison of the EHT polarimetric image of M87* on 2017 April 11 (left) with a representative ring model (right). Ticks show polarization fraction (color), magnitude (length), and position angle (direction); grayscale is identical for the two panels and shows total intensity of the EHT image of M87*. Ticks are only plotted where the M87* polarization exceeds 2% of the maximum intensity. All images are shown after convolution with a circular beam of FWHM 23 μas (shown in the left panel). As in Figure 8, the total intensity and polarization are individually normalized for each panel. The ring model has clockwise rotation with radial inflow, corresponding to the top left model in Figure 6 after counterclockwise rotation by 288°. For complete model details, see Section 5.1. The fractional polarization of the resolved ring model is set to 70%; the fractional polarization is reduced only through beam depolarization. Even after blurring, the ring model has significantly higher fractional polarization than the M87* image, although the relative variation in fractional polarization is similar across both images.

5.1. Comparison to the M87 Polarized Image

Recent EHT observations produced polarized images of M87* (EHTC VII). As reported in the one-zone model comparisons performed in EHTC V and EHTC VIII, the brightness, angular size, and expectation of significant Faraday effects coarsely constrain the magnetic field strength B, electron number density n_e, and electron temperature T_e in the flow imaged by the EHT. The EHTC VIII results suggest that $B \lesssim 30$ G, $10^4 < n_e < 10^7\,\mathrm{cm}^{-3}$, and $10^{10} < T_e < 1.2 \times 10^{11}$ K. The reconstructed images in EHTC VII were compared to general relativistic magnetohydrodynamic (GRMHD) simulations to identify a space of favored model parameters (EHTC VIII). We will now explore whether our ring model can reproduce the polarization structure in these favored GRMHD simulations and in EHT images of M87*.

For the GRMHD comparison, we first perform an azimuthal and temporal averaging in the fluid domain to approximate a stationary axisymmetric flow. In the fluid frame, the magnetic field in each cell is decomposed in Cartesian Kerr–Schild coordinates, which are then recast into cylindrical coordinates and then azimuthally averaged. These azimuthally averaged magnetic field decompositions are then further averaged over time between $7500 \leqslant t/(GM/c^3) \leqslant 10000$ (the final quarter of these simulations). We then sample values of the fluid velocity and magnetic field vectors from the averaged simulations and use these values to generate ring models at $\theta_0 = 17°$. To avoid sampling near where the tangential and radial field directions tend to abruptly flip sign, we use $z = 1M$, just above the midplane. We use $R = 4.5M$, corresponding to the apparent lensed size of the emission ring in EHT images of M87* (see the later discussion of the observed image). To create an image from the one-dimensional ring model, we adopt a radial profile that decays symmetrically in R about $R = 4.5$ as an exponential with a scale width of $2M$ (EHT images only constrain this width to be $< 5M$; EHTC VI). We take a pixel-wise fractional polarization $|m|$ of 0.7 before blurring in the ring model. Finally, we convolve both the ring model image and the GRMHD image with a 20 μas Gaussian kernel.

Using this approach, Figure 8 compares four favored GRMHD models to the corresponding ring models. In each case, the ring model reproduces the sense of EVPA twist and relative polarized intensity of the averaged and blurred GRMHD image, although discrepancies in $\arg(\beta_2)$ suggest contributions from emission away from the midplane or from other effects that are not included in the ring model (e.g., black hole spin or Faraday effects). The $R_{\rm low}$ and $R_{\rm high}$ parameters adapted from Mościbrodzka et al. (2016) for use in EHTC V tune the ratio of electron to ion temperatures depending on the magnetic energy density of the plasma; large values of $R_{\rm high}$ tend to produce significant emission far from the midplane, particularly in SANE models. Also, Faraday effects in MAD models can produce significant coherent rotation of the EVPA and, hence, in $\arg(\beta_2)$ (EHTC VIII).

Figure 9 compares a representative ring model to the "consensus" EHT polarimetric image for 2017 April 11 (i.e., the method-averaged image, see EHTC VII). The ring model parameters are chosen based on the observed image and a priori expectations for M87*. For simplicity, we take $B_z = 0$, although non-zero values of $B_z/B_{\rm eq}$ over a modest range also give similar results. We use $\chi = -150°$, to roughly match the observed β_2 for M87* (see Section 4.5). We take $R = d/(2\theta_{\rm g}) - 1 \approx 4.5$ (Section 4.1 explains the -1 factor), where $d \approx 42$ μas is the observed ring diameter and $\theta_g \approx 3.8$ μas is the angular gravitational radius (EHTC VI). We use $\beta = 0.4$, which is comparable to the equatorial velocity seen in GRMHD simulations (see Ricarte et al. 2020). We use $\theta_0 = 20°$ to match the jet inclination of M87*. Thus, this model has a modestly relativistic fluid with clockwise rotation and predominantly radial infall. This model corresponds to the top left panel of Figure 6 after rotation to match the jet position angle of M87*,

288°. As with the GRMHD comparison, the ring model is evaluated over an exponential profile with a scale width of $2\,M$ centered at $R = 4.5\ M$. The resulting ring model image is broadly consistent with the polarization morphology of the EHT image.

Although the qualitative agreement in Figure 9 is encouraging, our simple ring model fundamentally fails to reproduce all the features in the M87* image. Namely, our simplest model would produce a high fractional polarization ($\gtrsim$60%), while the M87* image has a low resolved fractional polarization $\lesssim$20%. This suggests that significant depolarization from internal Faraday effects are essential when modeling and interpreting the M87* image. Nevertheless, the success of the ring model in reproducing the structure of some GRMHD images that have significant Faraday effects is encouraging for the prospects of physical inference from this simple model.

One possibility for using our model for a more complex emission scenario is to combine multiple ring models that correspond to different emission regions. Specifically, the assumption $\eta = \chi + \pi$ corresponds to emission sourced by entrained magnetic field lines on the near side of the accretion flow (see Section 3.5). The far side of the flow would instead have $\eta = \chi$, flipping $\boldsymbol{B}_{\rm eq}$. Ignoring that contribution is equivalent to assuming that Faraday depolarization effects in the midplane are strong, so that the far-side emission is fully depolarized (as indicated in many models considered in EHTC VIII; see Ricarte et al. 2020). Our ring model could also be adapted to the case of weak Faraday rotation in the midplane; the resulting image would be the sum of two ring models, one with $\eta = \chi$ and the other with $\eta = \chi + \pi$. Both cases would reduce the image polarization substantially and may give better agreement with the M87* image, but we defer a full analysis to a future paper.

5.2. Comparison to Sgr A* Polarization

The polarization of Sgr A* shows continuous variability in the submillimeter (Marrone et al. 2006; Johnson et al. 2015; Bower et al. 2018) and also shows rapid variability during near-infrared (NIR) flares (Eckart et al. 2006; Trippe et al. 2007; Zamaninasab et al. 2010; Gravity Collaboration et al. 2018b). The variability often appears as "loops" in Stokes Q–U, and is frequently attributed to localized emission from an orbiting "hotspot" (Broderick & Loeb 2005, 2006; Fish et al. 2009). For the case of NIR flares, Faraday effects, absorption, and background emission are insignificant, so we can directly compare observed values of polarization and centroid motion with a simulated hotspot-only model.

Figure 10 shows a representative example. In this figure, we compute the hotspot polarized flux in the (Q, U) plane over a full period for a set of orbits with varying emission radius and inclination. We hold the underlying magnetic field structure to be vertical and constant, and adopt a relativistic Keplerian velocity for the hotspot: $\beta = 1/\sqrt{r-2}$. Our results are similar to previous studies with fully numerical calculations (see, e.g., Fish et al. 2009; Gravity Collaboration et al. 2018a, 2020); lensing and aberration compress the image of azimuthal evolution of polarization on one side of the flow and expand it on the other. In the formalism of azimuthal Fourier modes on the ring (Palumbo et al. 2020), power is shifted from the $m = 2$ mode to the $m = 1$ mode.

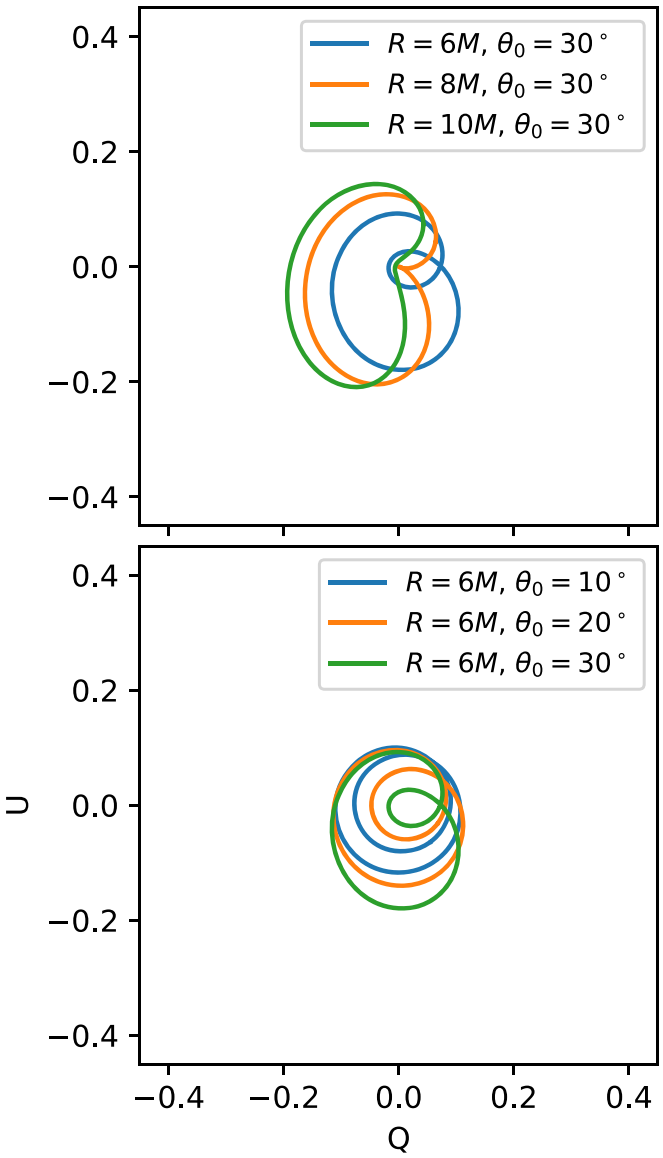

Figure 10. Polarization signatures for a vertically magnetized hotspot on a circular, relativistic Keplerian orbit. Each curve shows the polarized flux for a full orbit. Different curves correspond to varying the hotspot radius (top) and viewing inclination (bottom). Note that we use radio astronomy conventions for Q and U here, distinct from those in Equation (D10) by an overall sign.

6. Summary

We have developed an analytical method for computing the polarized image of a synchrotron-emitting fluid ring orbiting a Schwarzchild black hole. Given simple assumptions for the magnetic field geometry and fluid velocity, this model allows us to generate predictions of EVPA and relative polarized intensity as a polar function in the observed image at arbitrary viewing inclination. We explored the main features of the model through a number of representative examples and by further expansion in the inverse emission radius (lensing), fluid velocity (Doppler and aberration), and observer inclination (ring tilt). These reveal how the various physical effects influence the polarized image.

In its simplest form, the fractional polarization of our model is significantly higher than that seen in EHT images of M87* (EHTC VII). This may indicate significant sub-beam

depolarization, potentially from strong internal Faraday effects (EHTC VIII). If so, observations at higher frequencies, where Faraday effects are suppressed, may show significantly higher image polarizations, while observations at lower frequencies are expected to show a heavily depolarized "core."

Our polarized ring model provides intuition and insights about how a black hole's accretion flow and spacetime combine to produce a polarized image. It also provides a pathway to constrain these physical properties through direct comparisons with data and images from the EHT, GRAVITY, and future X-ray polarimetry studies. Extensions such as non-axisymmetric structure and non-equatorial emission will provide an expanded class of geometrical models to complement the growing library of GRMHD simulations (EHTC V). The inclusion of black hole spin will be necessary for rigorous understanding of M87* polarization, particularly if emission at small radii is significant. Further studies which examine the capability of the model in matching snapshots of GRMHD simulations with similar magnetic field and flow conditions will elucidate how readily field geometries may be directly inferred from polarized images.

We thank the National Science Foundation (awards OISE-1743747, AST-1816420, AST-1716536, AST-1440254, AST-1935980) and the Gordon and Betty Moore Foundation (GBMF-5278) for financial support of this work. This work was supported in part by the black hole Initiative, which is funded by grants from the John Templeton Foundation and the Gordon and Betty Moore Foundation to Harvard University. Support for this work was also provided by the NASA Hubble Fellowship grant HST-HF2-51431.001-A awarded by the Space Telescope Science Institute, which is operated by the Association of Universities for Research in Astronomy, Inc., for NASA, under contract NAS5-26555. The Event Horizon Telescope Collaboration thanks the following organizations and programs: the Academy of Finland (projects 274477, 284495, 312496, 315721); the Agencia Nacional de Investigación y Desarrollo (ANID), Chile via NCN19_058 (TITANs) and Fondecyt 3190878, the Alexander von Humboldt Stiftung; an Alfred P. Sloan Research Fellowship; Allegro, the European ALMA Regional Centre node in the Netherlands, the NL astronomy research network NOVA and the astronomy institutes of the University of Amsterdam, Leiden University and Radboud University; the black hole Initiative at Harvard University, through a grant (60477) from the John Templeton Foundation; the China Scholarship Council; Consejo Nacional de Ciencia y Tecnología (CONACYT, Mexico, projects U0004-246083, U0004-259839, F0003-272050, M0037-279006, F0003-281692, 104497, 275201, 263356); the Delaney Family via the Delaney Family John A. Wheeler Chair at Perimeter Institute; Dirección General de Asuntos del Personal Académico—Universidad Nacional Autónoma de México (DGAPA—UNAM, projects IN112417 and IN112820); the European Research Council Synergy Grant "BlackHoleCam: Imaging the Event Horizon of Black Holes" (grant 610058); the Generalitat Valenciana postdoctoral grant APOSTD/2018/177 and GenT Program (project CIDEGENT/2018/021); MICINN Research Project PID2019-108995GB-C22; the Gordon and Betty Moore Foundation (grant GBMF-3561; the Istituto Nazionale di Fisica Nucleare (INFN) sezione di Napoli, iniziative specifiche TEONGRAV; the International Max Planck Research School for Astronomy and Astrophysics at the Universities of Bonn and Cologne; Joint Princeton/Flatiron and Joint Columbia/Flatiron Postdoctoral Fellowships, research at the Flatiron Institute is supported by the Simons Foundation; the Japanese Government (Monbukagakusho: MEXT) Scholarship; the Japan Society for the Promotion of Science (JSPS) Grant-in-Aid for JSPS Research Fellowship (JP17J08829 and JP19H01943); the Key Research Program of Frontier Sciences, Chinese Academy of Sciences (CAS, grants QYZDJ-SSW-SLH057, QYZDJSSW- SYS008, ZDBS-LY-SLH011); the Leverhulme Trust Early Career Research Fellowship; the Max-Planck-Gesellschaft (MPG); the Max Planck Partner Group of the MPG and the CAS; the MEXT/JSPS KAKENHI (grants 18KK0090, JP18K13594, JP18K03656, JP18H03721, 18K03709, 18H01245, 25120007); the Malaysian Fundamental Research Grant Scheme (FRGS) FRGS/1/2019/STG02/UM/02/6; the MIT International Science and Technology Initiatives (MISTI) Funds; the Ministry of Science and Technology (MOST) of Taiwan (105-2112-M-001-025-MY3, 106-2112-M-001-011, 106-2119- M-001-027, 107-2119-M-001-017, 107-2119-M-001-020,107-2119-M-110-005, 108-2112-M-001-048, and 109-2124-M-001-005); the National Aeronautics and SpaceAdministration (NASA grant NNX17AL82G, Fermi Guest Investigator grant 80NSSC20K1567, NASA Astrophysics Theory Program grant 80NSSC20K0527, NASA NuSTAR award 80NSSC20K0645); the National Institute of Natural Sciences (NINS) of Japan; the National Key Research and Development Program of China (grant 2016YFA0400704, 2016YFA0400702); the National Science Foundation (NSF, grants AST-0096454, AST-0352953, AST-0521233, AST-0705062, AST-0905844, AST-0922984, AST-1126433, AST-1140030, DGE-1144085, AST-1207704, AST-1207730, AST-1207752, MRI-1228509, OPP-1248097, AST-1310896, AST-1555365, AST-1615796, AST-1715061, AST-1716327, AST-1903847, AST-2034306); the Natural Science Foundation of China (grants 11573051, 11633006, 11650110427, 10625314, 11721303, 11725312, 11933007, 11991052, 11991053); a fellowship of China Postdoctoral Science Foundation (2020M671266); the Natural Sciences and Engineering Research Council of Canada (NSERC, including a Discovery Grant and the NSERC Alexander Graham Bell Canada Graduate Scholarships-Doctoral Program); the National Research Foundation of Korea (the Global PhD Fellowship Grant: grants NRF-2015H1A2A1033752, 2015-R1D1A1A01056807, the Korea Research Fellowship Program: NRF-2015H1D3A1066561, Basic Research Support Grant 2019R1F1A1059721); the Netherlands Organization for Scientific Research (NWO) VICI award (grant 639.043.513) and Spinoza Prize SPI 78-409; the New Scientific Frontiers with Precision Radio Interferometry Fellowship awarded by the South African Radio Astronomy Observatory (SARAO), which is a facility of the National Research Foundation (NRF), an agency of the Department of Science and Innovation (DSI) of South Africa; the South African Research Chairs Initiative of the Department of Science and Innovation and National Research Foundation; the Onsala Space Observatory (OSO) national infrastructure, for the provisioning of its facilities/observational support (OSO receives funding through the Swedish Research Council under grant 2017-00648) the Perimeter Institute for Theoretical Physics (research at Perimeter Institute is supported by the Government of Canada through the Department of Innovation, Science and Economic Development and by the Province of Ontario through the Ministry of Research, Innovation and Science); the Spanish Ministerio de Economía y Competitividad (grants PGC2018-098915-B-C21,

AYA2016-80889-P, PID2019-108995GB-C21); the State Agency for Research of the Spanish MCIU through the "Center of Excellence Severo Ochoa" award for the Instituto de Astrofísica de Andalucía (SEV-2017-0709); the Toray Science Foundation; the Consejería de Economía, Conocimiento, Empresas y Universidad of the Junta de Andalucía (grant P18-FR-1769), the Consejo Superior de Investigaciones Científicas (grant 2019AEP112); the US Department of Energy (USDOE) through the Los Alamos National Laboratory (operated by Triad National Security, LLC, for the National Nuclear Security Administration of the USDOE (Contract 89233218CNA000001); the European Union's Horizon 2020 research and innovation program under grant agreement No. 730562 RadioNet; ALMA North America Development Fund; the Academia Sinica; Chandra DD7-18089X and TM6-17006X; the GenT Program (Generalitat Valenciana) Project CIDEGENT/2018/021. This work used the Extreme Science and Engineering Discovery Environment (XSEDE), supported by NSF grant ACI-1548562, and CyVerse, supported by NSF grants DBI-0735191, DBI-1265383, and DBI-1743442. XSEDE Stampede2 resource at TACC was allocated through TG-AST170024 and TG-AST080026N. XSEDE JetStream resource at PTI and TACC was allocated through AST170028. The simulations were performed in part on the SuperMUC cluster at the LRZ in Garching, on the LOEWE cluster in CSC in Frankfurt, and on the HazelHen cluster at the HLRS in Stuttgart. This research was enabled in part by support provided by Compute Ontario (http://computeontario.ca), Calcul Quebec (http://www.calculquebec.ca) and Compute Canada (http://www.computecanada.ca). We thank the staff at the participating observatories, correlation centers, and institutions for their enthusiastic support. This paper makes use of the following ALMA data: ADS/JAO.ALMA#2016.1.01154.V. ALMA is a partnership of the European Southern Observatory (ESO; Europe, representing its member states), NSF, and National Institutes of Natural Sciences of Japan, together with National Research Council (Canada), Ministry of Science and Technology (MOST; Taiwan), Academia Sinica Institute of Astronomy and Astrophysics (ASIAA; Taiwan), and Korea Astronomy and Space Science Institute (KASI; Republic of Korea), in cooperation with the Republic of Chile. The Joint ALMA Observatory is operated by ESO, Associated Universities, Inc. (AUI)/NRAO, and the National Astronomical Observatory of Japan (NAOJ). The NRAO is a facility of the NSF operated under cooperative agreement by AUI. APEX is a collaboration between the Max-Planck-Institut für Radioastronomie (Germany), ESO, and the Onsala Space Observatory (Sweden). The SMA is a joint project between the SAO and ASIAA and is funded by the Smithsonian Institution and the Academia Sinica. The JCMT is operated by the East Asian Observatory on behalf of the NAOJ, ASIAA, and KASI, as well as the Ministry of Finance of China, Chinese Academy of Sciences, and the National Key R&D Program (No. 2017YFA0402700) of China. Additional funding support for the JCMT is provided by the Science and Technologies Facility Council (UK) and participating universities in the UK and Canada. The LMT is a project operated by the Instituto Nacional de Astrofísica, Óptica, y Electrónica (Mexico) and the University of Massachusetts at Amherst (USA), with financial support from the Consejo Nacional de Ciencia y Tecnología and the National Science Foundation. The IRAM 30 m telescope on Pico Veleta, Spain is operated by IRAM and supported by CNRS (Centre National de la Recherche Scientifique, France), MPG (Max-Planck- Gesellschaft, Germany) and IGN (Instituto Geográfico Nacional, Spain). The SMT is operated by the Arizona Radio Observatory, a part of the Steward Observatory of the University of Arizona, with financial support of operations from the State of Arizona and financial support for instrumentation development from the NSF. The SPT is supported by the National Science Foundation through grant PLR- 1248097. Partial support is also provided by the NSF Physics Frontier Center grant PHY-1125897 to the Kavli Institute of Cosmological Physics at the University of Chicago, the Kavli Foundation and the Gordon and Betty Moore Foundation grant GBMF 947. The SPT hydrogen maser was provided on loan from the GLT, courtesy of ASIAA. The EHTC has received generous donations of FPGA chips from Xilinx Inc., under the Xilinx University Program. The EHTC has benefited from technology shared under open-source license by the Collaboration for Astronomy Signal Processing and Electronics Research (CASPER). The EHT project is grateful to T4Science and Microsemi for their assistance with Hydrogen Masers. This research has made use of NASA's Astrophysics Data System. We gratefully acknowledge the support provided by the extended staff of the ALMA, both from the inception of the ALMA Phasing Project through the observational campaigns of 2017 and 2018. We would like to thank A. Deller and W. Brisken for EHT-specific support with the use of DiFX. We acknowledge the significance that Maunakea, where the SMA and JCMT EHT stations are located, has for the indigenous Hawaiian people.

Appendix A
Accuracy of The Beloborodov Approximation

The model developed in Section 2 relies on the approximate formula Equation (4) derived by Beloborodov (2002). This approximation provides an estimate for α (and, equivalently, for ρ; Equation (C4)) for given emission coordinates R and ϕ. We now quantify the accuracy of this approximation.

Emission from the equatorial plane arriving at a given observer inclination angle $0 \leqslant \theta_o \leqslant \pi/2$ will sweep through $\psi \in [\pi/2 \pm \theta_o]$ as the azimuthal angle ϕ varies (see Equation (1)). In particular, all emission from a face-on disk has $\psi = \pi/2$, while emission from an edge-on disk samples angles $0 \leqslant \psi \leqslant \pi$. As the left panel in Figure 11 shows, the error in the Beloborodov approximation increases with ψ. In the context of the ring model, the approximation is most accurate at small inclinations. For $\theta_o = 17°$ for example (relevant for M87*), the approximation for ρ has a fractional error smaller than 2% for all values of R. This error decreases rapidly as ρ grows; e.g., for $\rho = 9$, the fractional error in ρ is smaller than 0.03%. In general, for emission on the side of the accretion disk closer to the observer (i.e., $\pi < \phi < 2\pi$, $\psi < \pi/2$), the approximation for ρ will have fractional error smaller than 0.6% for all $\rho \geqslant 3$ and any inclination. The error is larger for points on the far side of the ring ($0 < \phi < \pi$, $\psi > \pi/2$). However, even at an inclination angle of 60°, the accuracy is quite adequate, as shown by the right panel in Figure 11.

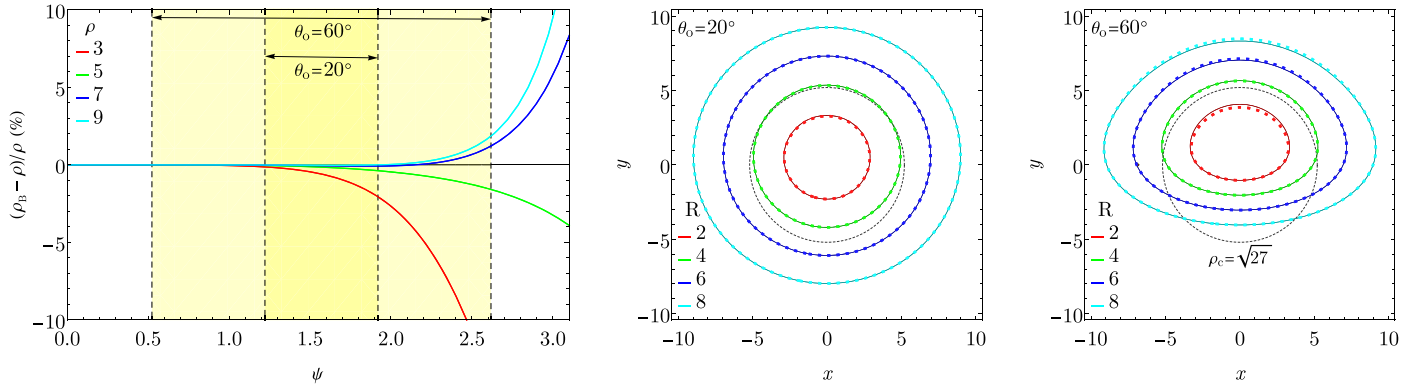

Figure 11. Testing the accuracy of the Beloborodov approximation. The left panel shows fractional error in $\rho = \sqrt{x^2 + y^2}$ as a function of ψ for $\rho = 3$, 5, 7, and 9. Yellow ranges denote values of ψ relevant for observer inclinations $\theta_o = 20°$ and 60°. The center and right panels show the image coordinates for rings with emission radius $R = 2$ (red), 4 (green), 6 (blue), and 8 (cyan) viewed at inclinations of 20° and 60°, respectively. For each ring, the solid line shows the exact calculation, while the dotted line shows the Beloborodov approximation (see Equation (C4)). The black dotted line shows the critical curve, $\rho = \rho_c \equiv \sqrt{27}$.

Appendix B
Transformations of Field Components

In the analysis given in the main text, we assumed that the magnetic field components B_r, B_ϕ, B_z are specified in the fluid frame. Under the usual assumptions of ideal MHD, the electric field vanishes in this frame: $E_r = E_\phi = E_z = 0$. Alternatively, we might wish to work with field components in the P-frame: $B_r^{(P)}$, $B_\phi^{(P)}$, $B_z^{(P)}$, $E_r^{(P)}$, $E_\phi^{(P)}$, $E_z^{(P)}$ (the electric field does not vanish in this frame).

The two frames are related by a Lorentz transformation with velocity $\boldsymbol{\beta}$ (expressed in terms of β and χ, see Equation (8)). The transformation is most transparent when we rewrite the radial and tangential field components in terms of "parallel" and "perpendicular" field components relative to the velocity:

$$B_\parallel^{(P)} = \cos\chi\, B_r^{(P)} + \sin\chi\, B_\phi^{(P)}, \qquad B_\perp^{(P)} = -\sin\chi\, B_r^{(P)} + \cos\chi\, B_\phi^{(P)}, \tag{B1}$$

$$B_r^{(P)} = \cos\chi\, B_\parallel^{(P)} - \sin\chi\, B_\perp^{(P)}, \qquad B_\phi^{(P)} = \sin\chi\, B_\parallel^{(P)} + \cos\chi\, B_\perp^{(P)}, \tag{B2}$$

with similar expressions for $\boldsymbol{E}^{(P)}$ and $\boldsymbol{B}$. The transformation rules are then

$$B_\parallel = B_\parallel^{(P)}, \qquad E_\parallel = E_\parallel^{(P)}, \tag{B3}$$

$$B_\perp = \gamma\, B_\perp^{(P)} + \beta\gamma E_z^{(P)}, \qquad B_z = \gamma\, B_z^{(P)} - \beta\gamma E_\perp^{(P)}, \tag{B4}$$

$$B_\perp^{(P)} = \gamma\, B_\perp - \beta\gamma E_z, \qquad B_z^{(P)} = \gamma\, B_z + \beta\gamma E_\perp, \tag{B5}$$

$$E_\perp = \gamma\, E_\perp^{(P)} - \beta\gamma B_z^{(P)}, \qquad E_z = \gamma\, E_z^{(P)} + \beta\gamma B_\perp^{(P)}, \tag{B6}$$

$$E_\perp^{(P)} = \gamma\, E_\perp + \beta\gamma B_z, \qquad E_z^{(P)} = \gamma\, E_z - \beta\gamma B_\perp, \tag{B7}$$

where, as usual, $\gamma = (1 - \beta^2)^{-1/2}$.

Using the above transformations, if we are given B_r, B_ϕ, B_z in the fluid frame, we can solve for $\boldsymbol{B}^{(P)}$ and $\boldsymbol{E}^{(P)}$ in the P-frame:

$$B_r^{(P)} = (\cos^2\chi + \gamma\sin^2\chi)B_r - (\gamma - 1)\cos\chi\sin\chi\, B_\phi, \tag{B8}$$

$$B_\phi^{(P)} = -(\gamma - 1)\cos\chi\sin\chi\, B_r + (\sin^2\chi + \gamma\cos^2\chi)B_\phi, \tag{B9}$$

$$B_z^{(P)} = \gamma\, B_z, \tag{B10}$$

$$E_r^{(P)} = -\beta\gamma\sin\chi\, B_z, \tag{B11}$$

$$E_\phi^{(P)} = \beta\gamma\cos\chi\, B_z, \tag{B12}$$

$$E_z^{(P)} = \beta\gamma\sin\chi\, B_r - \beta\gamma\cos\chi\, B_\phi. \tag{B13}$$

Similarly, if we are given the magnetic field components in the P-frame, we can solve for the other field components:

$$B_r = [\cos^2\chi + (1/\gamma)\sin^2\chi]B_r^{(P)} + ((\gamma - 1)/\gamma)\cos\chi\sin\chi B_\phi^{(P)}, \tag{B14}$$

$$B_\phi = ((\gamma - 1)/\gamma)\cos\chi\sin\chi B_r^{(P)} + [\sin^2\chi + (1/\gamma)\cos^2\chi]B_\phi^{(P)}, \tag{B15}$$

$$B_z = (1/\gamma)B_z^{(P)}, \tag{B16}$$

$$E_r^{(P)} = -\beta\sin\chi B_z^{(P)}, \tag{B17}$$

$$E_{\phi}^{(\mathrm{P})} = \beta \cos\chi B_z^{(\mathrm{P})}, \tag{B18}$$

$$E_z^{(\mathrm{P})} = \beta \sin\chi B_r^{(\mathrm{P})} - \beta \cos\chi B_{\phi}^{(\mathrm{P})}. \tag{B19}$$

These transformations are provided here for the convenience of readers who might prefer to work with field components in the Schwarzschild frame.

Appendix C
Emission Location versus Observed Coordinates

The radiation emitted by the point P in the ring at (R, ϕ) reaches the observer at sky coordinates (x, y), which we can write in terms of polar coordinates (ρ, φ) as described in Equation (28). Here we work out the relation between these two coordinates.

The relation between φ and ϕ is straightforward. Since the observer frame is tilted with respect to the ring plane by a rotation angle θ_o around the line of nodes, and since the geodesic lies entirely on a plane (because we have limited our analysis to the Schwarzschild spacetime), we find

$$\tan\varphi = \tan\phi \cos\theta_o. \tag{C1}$$

This relation can be used to translate ϕ to φ and vice versa. For the analysis in Appendix D, it is useful to express φ in terms of ϕ up to quadratic order. The corresponding relations are

$$\sin\phi \rightarrow \sin\varphi + (1/2)\sin^2\theta_o \sin\varphi\cos^2\varphi, \quad \cos\phi \rightarrow \cos\varphi - (1/2)\sin^2\theta_o\cos\varphi\sin^2\varphi. \tag{C2}$$

To calculate the mapping between R and ρ, consider the G-frame (Figure 1), where the geodesic lies in the xz-plane. At the emission point $(x, y, z) = (R, 0, 0)$, the geodesic makes an angle α with respect to the x-axis, where α is given by the Beloborodov approximation (4). Since the angular momentum around the y-axis in the G-frame is conserved, we have

$$\rho = k_{\phi} = Rk^{\hat{\phi}} = \frac{R\sin\alpha}{\left(1 - \frac{2}{R}\right)^{1/2}}. \tag{C3}$$

Squaring both sides,

$$\rho^2 = \frac{R^2(1-\cos^2\alpha)}{\left(1-\frac{2}{R}\right)} = R^2(1 - \sin^2\theta_o\sin^2\phi) + 2R(1 + \sin^2\theta_o\sin^2\phi + 2\sin\theta_o\sin\phi). \tag{C4}$$

This directly gives ρ in terms of R and ϕ; conversely, the quadratic equation can be solved to obtain R for a given ρ and ϕ. Equation (C4) is exact, except for the fact that we used the Beloborodov approximation (4) for $\cos\alpha$.

Since $(\partial\varphi/\partial R)_{\phi} = 0$, the Jacobian determinant $|J|$, which describes the transformation of differential area elements between (R, ϕ) and (ρ, φ), is given by

$$|J| = \left(\frac{\partial\rho}{\partial R}\right)_{\phi}\left(\frac{\rho\partial\varphi}{R\partial\phi}\right)_R = \frac{1}{R}[(R+1) - (R-1)\sin^2\theta_o\sin^2\phi + 2\sin\theta_o\sin\phi]\left(\frac{\sec^2\phi\cos\theta_o}{1+\tan^2\phi\cos^2\theta_o}\right). \tag{C5}$$

Appendix D
Series Expansion to Quadratic Order

The analysis in Section 2 is exact, modulo the Beloborodov approximaton, and is convenient for numerical calculations. However, for analytical studies, we need simpler relations. For this, we expand all the equations up to second order, treating the quantities $\sin\theta_o$, β and $2/R$, which describe tilt, relativistic velocity and gravity, as being small.[131] The relevant series expansion results are given below. In each equation, the second-order terms are shown inside square brackets.

The observed coordinates (x, y) of the geodesic emitted at location (R, ϕ) in the ring are given by

$$x = (R+1)\cos\varphi + \left[-\frac{1}{2R}\cos\varphi + 2\sin\theta_o\sin\varphi\cos\varphi - \frac{R}{2}\sin^2\theta_o\sin^2\varphi\cos\varphi\right], \tag{D1}$$

$$y = (R+1)\sin\varphi + \left[-\frac{1}{2R}\sin\varphi + 2\sin\theta_o\sin^2\varphi - \frac{R}{2}\sin^2\theta_o\sin^3\varphi\right]. \tag{D2}$$

In deriving these results, we first evaluated Equation (22) and then made the substitutions given in Equation (C2). The latter substitution is made in all the subsequent results presented in this appendix; thus the results are expressed in terms of the observed azimuthal angle φ.

To quadratic order, the Doppler factor δ is

$$\delta = 1 - \frac{1}{R} - \left[\frac{\beta^2}{2} + \frac{1}{2R^2} - \frac{2\beta}{R}\cos\chi + \beta\sin\theta_o\sin(\chi+\varphi)\right]. \tag{D3}$$

Note that Doppler boost due to azimuthal velocity is described by the last term, $\beta \sin\theta_o \sin(\chi+\varphi)$, which appears only at second order in the small quantities $\sin\theta_o$ and β. This is one of the reasons for expanding the equations to quadratic order.

Assuming that the spectral index $\alpha_\nu = 1$, the intensity of the linear polarized radiation at the observer is given by Equation (15):

$$|P| = \delta^4\, l_p\, |\boldsymbol{B}|^2 \sin^2\zeta. \tag{D4}$$

Expanding to quadratic order, the term $|\boldsymbol{B}|^2 \sin^2\zeta$ is given by

$$\begin{aligned}|\boldsymbol{B}|^2\sin^2\zeta = B_{\rm eq}^2 &+ \left(2\sin\theta_o\sin(\eta+\varphi) - \frac{4}{R}\cos\eta + 2\beta\cos(\chi-\eta)\right)B_{\rm eq}B_z \\ &+ \Bigg[-\left(\sin\theta_o\sin(\eta+\varphi) - \frac{2}{R}\cos\eta + \beta\cos(\chi-\eta)\right)^2 B_{\rm eq}^2 \\ &+ \left(-\frac{4}{R}\sin\theta_o\sin\varphi + \frac{4}{R^2} + \sin^2\theta_o + 2\beta\sin\theta_o\sin(\chi+\varphi) - \frac{4\beta}{R}\cos\chi + \beta^2\right)B_z^2 \\ &- \frac{4}{R}\sin\theta_o\cos\eta\sin\varphi B_{\rm eq}B_z\Bigg].\end{aligned} \tag{D5}$$

We have written the result in terms of the parameters $B_{\rm eq}$, η, B_z of the magnetic field in the fluid frame (see Equation (11)). This is helpful for the discussion in Section 4. Note that, in the absence of any equatorial magnetic field, the only contributions are at the second order (because the only terms with B_z^2 are inside the square brackets). Since the observed intensity is directly proportional to $|\boldsymbol{B}|^2\sin^2\zeta$, we need to expand to quadratic order to handle models with pure B_z.

To quadratic order, the path length l_p in Equation (13) is

$$\frac{l_p}{H} = 1 + \frac{1}{2}\left[\beta^2 + \frac{4}{R^2} + \sin^2\theta_o + 2\beta\sin\theta_o\sin(\chi+\varphi) - \frac{4\beta}{R}\cos\chi - \frac{4}{R}\sin\theta_o\sin\varphi\right]. \tag{D6}$$

We calculate the linear polarized intensity $|P|$ as the product of the three terms, δ^4, l_p and $|\boldsymbol{B}|^2\sin^2\zeta$ (see Equation (D4)). This gives

$$\begin{aligned}|P(\varphi)| = &\left(1-\frac{4}{R}\right)(B_r^2+B_\phi^2) + 2(\sin\theta_o\cos\varphi + \beta\sin\chi)B_\phi B_z + 2\left(-\frac{2}{R} + \beta\cos\chi + \sin\theta_o\sin\varphi\right)B_z B_r \\ &+ \Bigg[\left(\frac{2}{R}\sin\theta_o\sin\varphi + \frac{2}{r^2} + \frac{1}{2}\sin^2\theta_o\cos 2\varphi + \frac{10\beta}{R}\cos\chi + \beta\sin\theta_o(\sin(\chi-\varphi) - 4\sin(\chi+\varphi)) - \frac{\beta^2}{2}(4+\cos 2\chi)\right)B_r^2 \\ &+ \left(-\frac{2}{r}\sin\theta_o\sin\varphi + \frac{6}{R^2} - \frac{1}{2}\sin^2\theta_o\cos 2\varphi - \beta\sin\theta_o(4\sin(\chi+\varphi) + \sin(\chi-\varphi)) + \frac{6\beta}{R}\cos\chi - \frac{\beta^2}{2}(4-\cos 2\chi)\right)B_\phi^2 \\ &+ \left(-\frac{4}{R}\sin\theta_o\sin\varphi + \frac{4}{R^2} + \sin^2\theta_o + 2\beta\sin\theta_o\sin(\chi+\varphi) - \frac{4\beta}{R}\cos\chi + \beta^2\right)B_z^2 \\ &+ \left(\frac{4}{R}\sin\theta_o\cos\varphi - \sin^2\theta_o\sin 2\varphi - 2\beta\sin\theta_o\cos(\chi-\varphi) + \frac{4\beta}{R}\sin\chi - \beta^2\sin 2\chi\right)B_r B_\phi \\ &+ \left(-\frac{8}{R}\sin\theta_o\cos\varphi - \frac{8\beta}{R}\sin\chi\right)B_\phi B_z + \left(-\frac{12}{R}\sin\theta_o\sin\varphi + \frac{16}{R^2} - \frac{8\beta}{R}\cos\chi\right)B_z B_r\Bigg],\end{aligned} \tag{D7}$$

where we have written the answer in terms of B_r, B_ϕ, B_z in the fluid frame.

The electric field components E_x, E_y, which are normalized such that they are proportional to $\sin\zeta\ |\boldsymbol{B}|$ (see Equation (25)), are

$$\begin{aligned}E_x = &-\sin\varphi\, B_r - \cos\varphi\, B_\phi - \left(\sin\theta_o - \frac{2}{R}\sin\varphi + \beta\sin(\chi+\varphi)\right)B_z \\ &+ \Bigg[\left(-\frac{2}{R}\sin\theta_o\sin^2\varphi + \frac{2}{R^2}\sin\varphi + \frac{1}{2}\sin^2\theta_o\sin^3\varphi + \frac{\beta}{2}\sin\theta_o(\cos\chi - \cos(\chi+2\varphi))\right. \\ &\left. - \frac{2\beta}{R}\sin(\chi+\varphi) + \frac{\beta^2}{4}(\sin\varphi + \sin(2\chi+\varphi))\right)B_r \\ &+ \left(-\frac{1}{R}\sin\theta_o\sin 2\varphi + \frac{1}{8}\sin^2\theta_o(5\cos\varphi - \cos 3\varphi) + \frac{\beta}{2}\sin\theta_o(\sin\chi + \sin(\chi+2\varphi))\right. \\ &\left. + \frac{\beta^2}{4}(\cos\varphi - \cos(2\chi+\varphi))\right)B_\phi \\ &+ \frac{2}{R}\sin\theta_o\sin^2\varphi\, B_z\Bigg],\end{aligned} \tag{D8}$$

$$
\begin{aligned}
E_y = {} & \cos\varphi\, B_r - \sin\varphi\, B_\phi + \left(-\frac{2}{R}\cos\varphi + \beta\cos(\chi+\varphi)\right)B_z \\
& + \left[\left(\frac{1}{R}\sin\theta_o \sin 2\varphi - \frac{2}{R^2}\cos\varphi - \frac{1}{8}\sin^2\theta_o(\cos\varphi - \cos 3\varphi) + \frac{\beta}{2}\sin\theta_o(\sin\chi - \sin(\chi+2\varphi))\right.\right. \\
& \quad \left.\left. + \frac{2\beta}{R}\cos(\chi+\varphi) - \frac{\beta^2}{4}(\cos\varphi + \cos(2\chi+\varphi))\right)B_r \right. \\
& + \left(\frac{2}{R}\sin\theta_o\cos^2\varphi - \frac{1}{8}\sin^2\theta_o(\sin\varphi + \sin 3\varphi) - \frac{\beta}{2}\sin\theta_o(\cos\chi + \cos(\chi+2\varphi))\right. \\
& \quad \left. + \frac{\beta^2}{4}(\sin\varphi - \sin(2\chi+\varphi))\right)B_\phi \\
& \left. - \frac{1}{R}\sin\theta_o\sin 2\varphi\, B_z\right]. \qquad \text{(D9)}
\end{aligned}
$$

From E_x, E_y, we can obtain the observed field components, $E_{x,\rm obs}$, $E_{y,\rm obs}$, from Equations (26), (27). We can then compute the Stokes parameters Q and U via

$$
Q = E_{x,\rm obs}^2 - E_{y,\rm obs}^2 = (E_x^2 - E_y^2)\delta^2\, l_{\rm p}^{1/2}, \qquad U = 2E_{x,\rm obs}E_{y,\rm obs} = 2E_xE_y\,\delta^2\, l_{\rm p}^{1/2}. \qquad \text{(D10)}
$$

We can also calculate $|P| = E_{x,\rm obs}^2 + E_{y,\rm obs}^2$, but this will simply reproduce the answer given in Equation (D7). We do not write down the results for Q and U as the expressions are large. Instead we define the complex polarization $P(\varphi)$ in the usual way (see Equation (29)), and expand it in a Fourier series as described in Palumbo et al. (2020),

$$
P(\varphi) \equiv Q(\varphi) + iU(\varphi) = \frac{1}{2\pi}\sum_{m=-\infty}^{\infty}\beta_m\, e^{im\varphi}. \qquad \text{(D11)}
$$

To zeroth and linear order there are only two non-zero coefficients, β_1 and β_2, and to quadratic order, there are five non-zero coefficients, $\beta_0 - \beta_4$. The expressions for these coefficients are given below (second-order contributions are shown inside square brackets):

$$
\beta_0 = \left[-\frac{1}{4}\sin^2\theta_o(B_r^2 + 3B_\phi^2 - 4B_z^2 - 2iB_rB_\phi)\right] \qquad \text{(D12)}
$$

$$
= \left[\frac{1}{4}\sin^2\theta_o(e^{2i\eta} - 2)B_{\rm eq}^2 + \sin^2\theta_o B_z^2\right], \qquad \text{(D13)}
$$

$$
\begin{aligned}
\beta_1 = {} & 2\sin\theta_o(-iB_r + B_\phi)B_z + \left[\left(-\frac{i}{R} + i\beta\left(\frac{3}{2}e^{-i\chi} + e^{i\chi}\right)\right)\sin\theta_o\, B_r^2 + \left(-\frac{3i}{R} + i\beta\left(-\frac{3}{2}e^{-i\chi} + e^{i\chi}\right)\right)\sin\theta_o\, B_\phi^2\right. \\
& \left. + \left(\frac{4i}{R} - 2i\beta e^{i\chi}\right)\sin\theta_o\, B_z^2 - \left(\frac{2}{R} + 3\beta e^{-i\chi}\right)\sin\theta_o\, B_rB_\phi - \frac{10}{R}\sin\theta_o\, B_\phi B_z + \frac{10i}{R}\sin\theta_o\, B_zB_r\right] \qquad \text{(D14)}
\end{aligned}
$$

$$
\begin{aligned}
= {} & -2i\sin\theta_o e^{i\eta}B_{\rm eq}B_z + \left[\left(-\frac{i}{R}(2 - e^{2i\eta})\sin\theta_o + i\beta\sin\theta_o\left(e^{i\chi} + \frac{3}{2}e^{i(2\eta-\chi)}\right)\right)B_{\rm eq}^2\right. \\
& \left. + \left(\frac{4i}{R} - 2i\beta e^{i\chi}\right)\sin\theta_o B_z^2 + \frac{10i}{R}\sin\theta_o e^{i\eta}B_{\rm eq}B_z\right], \qquad \text{(D15)}
\end{aligned}
$$

$$
\begin{aligned}
\beta_2 = {} & -\left(1 - \frac{4}{R}\right)(B_r + iB_\phi)^2 - 2\left(\beta e^{i\chi} - \frac{2}{R}\right)(B_r + iB_\phi)B_z \\
& + \left[\left(-\frac{2}{R^2} - \frac{i\beta}{R}(4\sin\chi - 10i\cos\chi) + \frac{\beta^2}{2}(4 + e^{2I\chi})\right)B_r^2\right. \\
& + \left(\frac{6}{R^2} + \frac{6\beta}{R}\cos\chi + \frac{\beta^2}{2}(-4 + e^{2i\chi})\right)B_\phi^2 \\
& + \left(-\frac{4}{R^2} + \frac{4\beta}{R}e^{i\chi} - \beta^2e^{2i\chi}\right)B_z^2 + \left(-\frac{8i}{R^2} + \frac{4\beta}{R}(\sin\chi - 4i\cos\chi) + 4i\beta^2\right)B_rB_\phi \\
& \left. + \left(-\frac{16i}{R^2} + \frac{8i\beta}{R}e^{i\chi}\right)B_\phi B_z + \left(-\frac{16}{R^2} + \frac{8\beta}{R}e^{i\chi}\right)B_zB_r\right] \qquad \text{(D16)}
\end{aligned}
$$

$$= -\left(1 - \frac{4}{R}\right)e^{2i\eta}B_{\rm eq}^2 + \left(\frac{4}{R}e^{i\eta} - 2\beta e^{i(\chi+\eta)}\right)B_{\rm eq}B_z$$
$$+ \left[\left(\frac{2}{R^2}(1 - 2e^{2i\eta}) + \frac{\beta^2}{2}(e^{2i\chi} + 4e^{2i\eta}) - \frac{\beta}{R}(e^{2i\eta}(6\cos\chi + 2e^{i\chi}) + 2e^{i\chi})\right)B_{\rm eq}^2\right.$$
$$\left. + \left(-\frac{4}{R^2} + \frac{4\beta}{R}e^{i\chi} - \beta^2 e^{2i\chi}\right)B_z^2 + \left(-\frac{16}{R^2}e^{i\eta} + \frac{8\beta}{R}e^{i(\chi+\eta)}\right)B_{\rm eq}B_z\right], \tag{D17}$$

$$\beta_3 = \left[\left(\frac{i}{R} - \frac{5i\beta}{2}e^{i\chi}\right)\sin\theta_{\rm o}(B_r + iB_\phi)^2 - \frac{2i}{R}\sin\theta_{\rm o}(B_r + iB_\phi)B_z\right] \tag{D18}$$

$$= \left[\left(\frac{i}{R} - \frac{5i\beta}{2}e^{i\chi}\right)\sin\theta_{\rm o}e^{2i\eta}B_{\rm eq}^2 - \frac{2i}{R}\sin\theta_{\rm o}e^{i\eta}B_{\rm eq}B_z\right], \tag{D19}$$

$$\beta_4 = \left[-\frac{1}{4}\sin^2\theta_{\rm o}(B_r + iB_\phi)^2\right] \tag{D20}$$

$$= \left[-\frac{1}{4}\sin^2\theta_{\rm o}e^{2i\eta}B_{\rm eq}^2\right]. \tag{D21}$$

For each β_m coefficient, we give the result both in terms of B_r, B_ϕ, B_z, and in terms of $B_{\rm eq}$, η, B_z.

ORCID iDs

Ramesh Narayan https://orcid.org/0000-0002-1919-2730
Daniel C. M. Palumbo https://orcid.org/0000-0002-7179-3816
Michael D. Johnson https://orcid.org/0000-0002-4120-3029
Zachary Gelles https://orcid.org/0000-0001-8053-4392
Angelo Ricarte https://orcid.org/0000-0001-5287-0452
Jason Dexter https://orcid.org/0000-0003-3903-0373
Charles F. Gammie https://orcid.org/0000-0001-7451-8935
Andrew A. Chael https://orcid.org/0000-0003-2966-6220
Kazunori Akiyama https://orcid.org/0000-0002-9475-4254
Juan Carlos Algaba https://orcid.org/0000-0001-6993-1696
Richard Anantua https://orcid.org/0000-0003-3457-7660
Mislav Baloković https://orcid.org/0000-0003-0476-6647
Lindy Blackburn https://orcid.org/0000-0002-9030-642X
Geoffrey C. Bower https://orcid.org/0000-0003-4056-9982
Hope Boyce https://orcid.org/0000-0002-6530-5783
Avery E. Broderick https://orcid.org/0000-0002-3351-760X
Thomas Bronzwaer https://orcid.org/0000-0003-1151-3971
Do-Young Byun https://orcid.org/0000-0003-1157-4109
Chi-kwan Chan https://orcid.org/0000-0001-6337-6126
Shami Chatterjee https://orcid.org/0000-0002-2878-1502
Ilje Cho https://orcid.org/0000-0001-6083-7521
Pierre Christian https://orcid.org/0000-0001-6820-9941
James M. Cordes https://orcid.org/0000-0002-4049-1882
Jordy Davelaar https://orcid.org/0000-0002-2685-2434
Gregory Desvignes https://orcid.org/0000-0003-3922-4055
Heino Falcke https://orcid.org/0000-0002-2526-6724
Joseph Farah https://orcid.org/0000-0003-4914-5625
Vincent L. Fish https://orcid.org/0000-0002-7128-9345
Ed Fomalont https://orcid.org/0000-0002-9036-2747
Per Friberg https://orcid.org/0000-0002-8010-8454
Antonio Fuentes https://orcid.org/0000-0002-8773-4933
Roberto García https://orcid.org/0000-0002-6584-7443
Ciriaco Goddi https://orcid.org/0000-0002-2542-7743
José L. Gómez https://orcid.org/0000-0003-4190-7613
Mark Gurwell https://orcid.org/0000-0003-0685-3621
Kazuhiro Hada https://orcid.org/0000-0001-6906-772X
Daryl Haggard https://orcid.org/0000-0001-6803-2138
Mareki Honma https://orcid.org/0000-0003-4058-9000
Shiro Ikeda https://orcid.org/0000-0002-2462-1448
Sara Issaoun https://orcid.org/0000-0002-5297-921X
Britton Jeter https://orcid.org/0000-0003-2847-1712
Svetlana Jorstad https://orcid.org/0000-0001-6158-1708
Mansour Karami https://orcid.org/0000-0001-7387-9333
Tomohisa Kawashima https://orcid.org/0000-0001-8527-0496
Garrett K. Keating https://orcid.org/0000-0002-3490-146X
Jae-Young Kim https://orcid.org/0000-0001-8229-7183
Jongsoo Kim https://orcid.org/0000-0002-1229-0426
Junhan Kim https://orcid.org/0000-0002-4274-9373
Motoki Kino https://orcid.org/0000-0002-2709-7338
Patrick M. Koch https://orcid.org/0000-0003-2777-5861
Shoko Koyama https://orcid.org/0000-0002-3723-3372
Michael Kramer https://orcid.org/0000-0002-4175-2271
Thomas P. Krichbaum https://orcid.org/0000-0002-4892-9586
Cheng-Yu Kuo https://orcid.org/0000-0001-6211-5581
Tod R. Lauer https://orcid.org/0000-0003-3234-7247
Sang-Sung Lee https://orcid.org/0000-0002-6269-594X
Kuo Liu https://orcid.org/0000-0002-2953-7376
Laurent Loinard https://orcid.org/0000-0002-5635-3345
Ru-Sen Lu (路如森) https://orcid.org/0000-0002-7692-7967
Sera Markoff https://orcid.org/0000-0001-9564-0876
Daniel P. Marrone https://orcid.org/0000-0002-2367-1080
Alan P. Marscher https://orcid.org/0000-0001-7396-3332
Iván Martí-Vidal https://orcid.org/0000-0003-3708-9611
Satoki Matsushita https://orcid.org/0000-0002-2127-7880
Lia Medeiros https://orcid.org/0000-0003-2342-6728

[131] Because the solution for the coordinate x involves a division by $\sin\theta_{\rm o}$, it is necessary to keep terms up to $\sin^3\theta_{\rm o}$ in the expressions leading up to this quantity.

Yosuke Mizuno https://orcid.org/0000-0002-8131-6730
Kotaro Moriyama https://orcid.org/0000-0003-1364-3761
Hiroshi Nagai https://orcid.org/0000-0003-0292-3645
Masanori Nakamura https://orcid.org/0000-0001-6081-2420
Joey Neilsen https://orcid.org/0000-0002-8247-786X
Roberto Neri https://orcid.org/0000-0002-7176-4046
Michael A. Nowak https://orcid.org/0000-0001-6923-1315
Gisela N. Ortiz-León https://orcid.org/0000-0002-2863-676X
Jongho Park https://orcid.org/0000-0001-6558-9053
Ue-Li Pen https://orcid.org/0000-0003-2155-9578
Dominic W. Pesce https://orcid.org/0000-0002-5278-9221
Richard Plambeck https://orcid.org/0000-0001-6765-9609
Oliver Porth https://orcid.org/0000-0002-4584-2557
Dimitrios Psaltis https://orcid.org/0000-0003-4058-2837
Hung-Yi Pu https://orcid.org/0000-0001-9270-8812
Venkatessh Ramakrishnan https://orcid.org/0000-0002-9248-086X
Ramprasad Rao https://orcid.org/0000-0002-1407-7944
Mark G. Rawlings https://orcid.org/0000-0002-6529-202X
Luciano Rezzolla https://orcid.org/0000-0002-1330-7103
Bart Ripperda https://orcid.org/0000-0002-7301-3908
Freek Roelofs https://orcid.org/0000-0001-5461-3687
Eduardo Ros https://orcid.org/0000-0001-9503-4892
David Sánchez-Arguelles https://orcid.org/0000-0002-7344-9920
Mahito Sasada https://orcid.org/0000-0001-5946-9960
Tuomas Savolainen https://orcid.org/0000-0001-6214-1085
Karl-Friedrich Schuster https://orcid.org/0000-0003-2890-9454
Lijing Shao https://orcid.org/0000-0002-1334-8853
Bong Won Sohn https://orcid.org/0000-0002-4148-8378
Paul Tiede https://orcid.org/0000-0003-3826-5648
Kenji Toma https://orcid.org/0000-0002-7114-6010
Sascha Trippe https://orcid.org/0000-0003-0465-1559
Daniel R. van Rossum https://orcid.org/0000-0001-7772-6131
Jan Wagner https://orcid.org/0000-0003-1105-6109
Derek Ward-Thompson https://orcid.org/0000-0003-1140-2761
Robert Wharton https://orcid.org/0000-0002-7416-5209
Maciek Wielgus https://orcid.org/0000-0002-8635-4242
George N. Wong https://orcid.org/0000-0001-6952-2147
Doosoo Yoon https://orcid.org/0000-0001-8694-8166
Guang-Yao Zhao https://orcid.org/0000-0002-4417-1659

References

Bardeen, J. 1973, in Black Holes, ed. C. Dewitt & B. S. Dewitt (New York: Gordon and Breach), 215
Beloborodov, A. M. 2002, ApJL, 566, L85
Bisnovatyi-Kogan, G. S. 2019, Univ, 5, 146
Blandford, R. D., & Königl, A. 1979, ApJ, 232, 34
Bower, G. C., Broderick, A., Dexter, J., et al. 2018, ApJ, 868, 101
Broderick, A. E., & Loeb, A. 2005, MNRAS, 363, 353
Broderick, A. E., & Loeb, A. 2006, MNRAS, 367, 905
Bromley, B. C., Melia, F., & Liu, S. 2001, ApJL, 555, L83
Carter, B. 1968, PhRv, 174, 1559
Connors, P. A., Piran, T., & Stark, R. F. 1980, ApJ, 235, 224
Eckart, A., Schödel, R., Meyer, L., et al. 2006, A&A, 455, 1
Event Horizon Telescope Collaboration, Akiyama, K., Alberdi, A., et al. 2019a, ApJL, 875, L1
Event Horizon Telescope Collaboration, Akiyama, K., Alberdi, A., et al. 2019b, ApJL, 875, L2
Event Horizon Telescope Collaboration, Akiyama, K., Alberdi, A., et al. 2019c, ApJL, 875, L3
Event Horizon Telescope Collaboration, Akiyama, K., Alberdi, A., et al. 2019d, ApJL, 875, L4
Event Horizon Telescope Collaboration, Akiyama, K., Alberdi, A., et al. 2019e, ApJL, 875, L5
Event Horizon Telescope Collaboration, Akiyama, K., Alberdi, A., et al. 2019f, ApJL, 875, L6
Event Horizon Telescope Collaboration, Akiyama, K., Algaba, J. C., et al. 2021a, ApJL, 910, L12
Event Horizon Telescope Collaboration, Akiyama, K., Algaba, J. C., et al. 2021b, ApJL, 910, L13
Fish, V. L., Doeleman, S. S., Broderick, A. E., Loeb, A., & Rogers, A. E. E. 2009, ApJ, 706, 1353
Gates, D. E. A., Hadar, S., & Lupsasca, A. 2020, PhRevD, 102, 104041
Gold, R., McKinney, J. C., Johnson, M. D., & Doeleman, S. S. 2017, ApJ, 837, 180
Gralla, S. E., & Lupsasca, A. 2020a, PhRvD, 101, 044031
Gralla, S. E., & Lupsasca, A. 2020b, PhRvD, 101, 044032
Gravity Collaboration, Abuter, R., Amorim, A., et al. 2018a, A&A, 618, L10
Gravity Collaboration, Abuter, R., Amorim, A., et al. 2018b, A&A, 615, L15
Gravity Collaboration, Jiménez-Rosales, A., Dexter, J., et al. 2020, A&A, 643, A56
Himwich, E., Johnson, M. D., Lupsasca, A. r., & Strominger, A. 2020, PhRvD, 101, 084020
Igumenshchev, I. V., Narayan, R., & Abramowicz, M. A. 2003, ApJ, 592, 1042
Jiménez-Rosales, A., & Dexter, J. 2018, MNRAS, 478, 1875
Johnson, M. D., Fish, V. L., Doeleman, S. S., et al. 2015, Sci, 350, 1242
Li, L.-X., Narayan, R., & McClintock, J. E. 2009, ApJ, 691, 847
Li, L.-X., Zimmerman, E. R., Narayan, R., & McClintock, J. E. 2005, ApJS, 157, 335
Mahadevan, R., Narayan, R., & Yi, I. 1996, ApJ, 465, 327
Marin, F., Dovčiak, M., Muleri, F., Kislat, F. F., & Krawczynski, H. S. 2018, MNRAS, 473, 1286
Marrone, D. P., Moran, J. M., Zhao, J.-H., & Rao, R. 2006, JPhCS, 54, 354
Mościbrodzka, M., Dexter, J., Davelaar, J., & Falcke, H. 2017, MNRAS, 468, 2214
Mościbrodzka, M., Falcke, H., & Shiokawa, H. 2016, A&A, 586, A38
Narayan, R., Igumenshchev, I. V., & Abramowicz, M. A. 2003, PASJ, 55, L69
Palumbo, D. C. M., Wong, G. N., & Prather, B. S. 2020, ApJ, 894, 156
Ricarte, A., Prather, B. S., Wong, G. N., et al. 2020, MNRAS, 498, 5468
Schnittman, J. D., & Krolik, J. H. 2009, ApJ, 701, 1175
Shcherbakov, R. V., Penna, R. F., & McKinney, J. C. 2012, ApJ, 755, 133
Tchekhovskoy, A., Narayan, R., & McKinney, J. C. 2011, MNRAS, 418, L79
Trippe, S., Paumard, T., Ott, T., et al. 2007, MNRAS, 375, 764
Walker, M., & Penrose, R. 1970, CMaPh, 18, 265
Walker, R. C., Hardee, P. E., Davies, F. B., Ly, C., & Junor, W. 2018, ApJ, 855, 128
Zamaninasab, M., Eckart, A., Witzel, G., et al. 2010, A&A, 510, A3